

See discussions, stats, and author profiles for this publication at: <https://www.researchgate.net/publication/258063216>

Lamellar Salt-Doped Hybrids with Two Reversible Order/Disorder Phase Transitions

ARTICLE in THE JOURNAL OF PHYSICAL CHEMISTRY B · OCTOBER 2013

Impact Factor: 3.3 · DOI: 10.1021/jp407366c · Source: PubMed

CITATIONS

3

READS

22

5 AUTHORS, INCLUDING:



S. C. Nunes

Universidade da Beira Interior

35 PUBLICATIONS 408 CITATIONS

SEE PROFILE



Rute A Sá Ferreira

University of Aveiro

336 PUBLICATIONS 6,203 CITATIONS

SEE PROFILE



Luís D Carlos

University of Aveiro

483 PUBLICATIONS 9,764 CITATIONS

SEE PROFILE



Verónica de Zea Bermudez

Universidade de Trás-os-Montes e Alto Douro

187 PUBLICATIONS 3,936 CITATIONS

SEE PROFILE

Lamellar Salt-Doped Hybrids with Two Reversible Order/Disorder Phase Transitions

Sílvia C. Nunes,^{*,†,‡} Rute A. S. Ferreira,[§] Luís D. Carlos,[§] Paulo Almeida,[†]
and Verónica de Zea Bermudez^{*,†,‡,||}

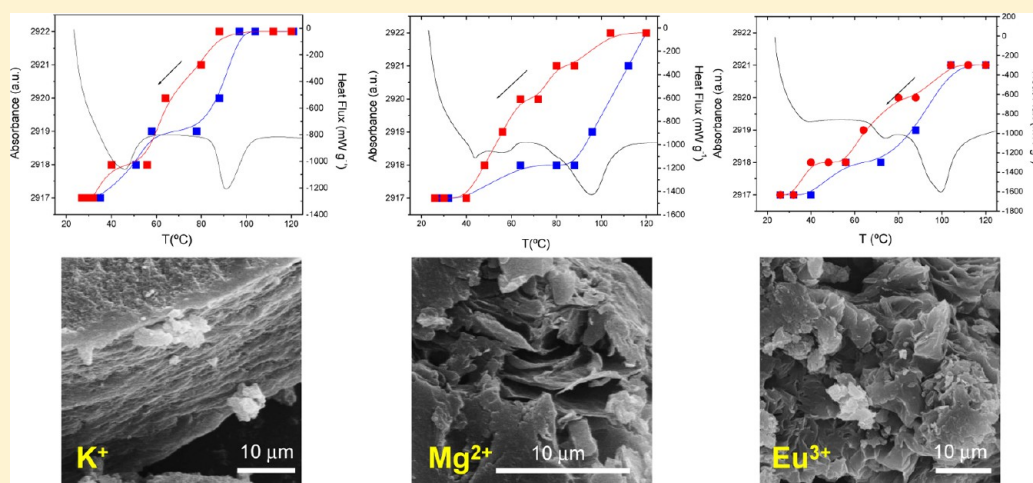
[†]Chemistry Department and CICS - Centro de Investigação em Ciências da Saúde, University of Beira Interior, 6200-001 Covilhã, Portugal

[‡]Chemistry Department, University of Trás-os-Montes and Alto Douro, 5001-801 Vila Real, Portugal

[§]Physics Department and CICECO, University of Aveiro, 3810-193 Aveiro, Portugal

^{||}CQ-VR, University of Trás-os-Montes e Alto Douro, 5001-801 Vila Real, Portugal

S Supporting Information



ABSTRACT: A lamellar bilayer hierarchically structured amide cross-linked alkyl/siloxane hybrid matrix (mono-amidosil, m-A(14)) was doped with a wide concentration range of potassium triflate (KCF_3SO_3), magnesium triflate ($\text{Mg}(\text{CF}_3\text{SO}_3)_2$), and europium triflate ($\text{Eu}(\text{CF}_3\text{SO}_3)_3$). In the K^+ , Mg^{2+} , and Eu^{3+} -based samples with $n \geq 5$, 20, and 60 (where n is the molar ratio of amide $\text{C}=\text{O}$ groups per cation), respectively, the original lamellar structure of m-A(14) coexists with a new lamellar phase with lower interlamellar distance. The texture of the mono-amidosils doped with K^+ , Mg^{2+} , and Eu^{3+} ions mimics cabbage leaves, foliated schist, and sea sponges, respectively. In the three series of materials, the cations bond to the oxygen atoms of the amide carbonyl groups. The amide–amide hydrogen-bonded array of m-A(14) is less perturbed by the inclusion of KCF_3SO_3 and $\text{Mg}(\text{CF}_3\text{SO}_3)_2$ than by the incorporation of $\text{Eu}(\text{CF}_3\text{SO}_3)_3$. The degree of ionic association is low for $n \geq 20$. The cations coordinate to the oxygen atoms of the triflate ions, forming contact ion pairs at higher salt content. In the $\text{Mg}(\text{CF}_3\text{SO}_3)_2$ - and $\text{Eu}(\text{CF}_3\text{SO}_3)_3$ -containing materials with $n = 5$ and 10, respectively, crystalline salt is formed. The structural changes undergone by the alkyl chains of selected mono-amidosils in a heating/cooling cycle are reversible, are time-independent, and exhibit two distinct hysteresis domains, one associated with the order/disorder phase transition of the original lamellar bilayer structure of m-A(14) and the second one associated with the order/disorder phase transition of the new lamellar bilayer structure formed in the presence of the salts.

INTRODUCTION

Nowadays the production of organic/inorganic hybrid^{1,2} nanostructures with exceptional control over size, shape, composition, and organization of nanoscale domains^{3–11} remains as a great challenge for the development of the next generation of well-ordered materials.^{12,13}

The combination of the sol–gel process¹⁴ with self-directed assembly routes is a suitable approach to synthesize organized

hybrid materials. Self-directed assembly occurs in the absence of external structure directing agents (or templates), since the supramolecular structure which grows as reactions proceed acts as an internal template. The driving forces of the whole process

Received: July 24, 2013

Revised: October 18, 2013

Published: October 21, 2013

are weak interactions (van der Waals and/or π - π interactions and/or hydrogen bonding). Typically ordered hybrids are formed from a homogeneous solution composed of a mixture of a bridged or non-bridged organosilane, water, an alcohol (or another solvent), and an acid. Many of the studies carried out have demonstrated that the efficient preparation of ordered nanostructured organic/inorganic hybrids relies on a judicious choice of the experimental synthesis conditions (e.g., water and alcohol contents, reaction time, type of solvent and catalyst, pH, and temperature) and of the chemical nature of the organic precursor.

A vast number of long-range ordered bridged silsesquioxanes (BSs) with hierarchical nanostructures and a myriad of well-defined morphologies at the macroscopic scale were produced via self-directed assembly of bridged organosilanes incorporating a cross-link prone to participating in hydrogen bonding interactions.^{15–26}

In contrast, just a few ordered non-bridged silsesquioxanes (NBSs) resulted upon application of the same synthesis strategy. The large majority of such materials were obtained from branched or non-branched alkoxy- or chlorosilanes carrying pendant alkyl chains and lacking any cross-links.^{27–37} The first hierarchically structured NBS incorporating an amide cross-link emerged from research in our group.^{38,39} This material, classed as mono-amidosil, was synthesized from the organosilane precursor $(\text{RO})_3\text{Si}-(\text{CH}_2)_3-\text{Y}-\text{R}'$ (where $\text{R} = \text{CH}_3\text{CH}_2$, $\text{Y} = \text{NHC}(=\text{O})$, and $\text{R}' = (\text{CH}_2)_{14}-\text{CH}_3$) and represented the first example of a photoluminescent bilayered lamellar suprastructure displaying a unique nanoscopic sensitivity. In the mono-amidosil m-A(14) (where m, A, and 14 represent mono, the amide group, and the number of CH_2 repeat units, respectively), self-directed assembly is governed by hydrogen bonding between the amide groups, tail-to-tail van der Waals interactions between the pendant all-*trans* alkyl chains assuming a partially interdigitated packing mode, and an entropic term related to the phase separation between the alkyl chains and the siloxane nanodomains. Interestingly, the alkyl chains of m-A(14) exhibit an order/disorder phase transition. This has an onset temperature of 92 °C and is reversible with a heating/cooling cycle operating between room temperature and 120 °C, inducing hysteretic behavior of the emission energy and the emergence of a thermally activated optical memory effect. The energetics of the order/disorder transition involves a synergy between van der Waals interactions and hydrogen bonding, i.e., the order/disorder transition in the alkyl chains determines and is also simultaneously constrained by the annihilation/formation of the amide–amide array. During heating, a contraction of the bilayer structure and an expansion of the siliceous layer occur (i.e., the interlamellar distance is deeply reduced and the characteristic distance associated with order within the siliceous domains increases, respectively), as the chains become disordered (*gauche* conformations) and the hydrogen-bonded amide–amide array is partially destroyed. During cooling, the rate of conformational recovery of the polymer chains is much faster than the rate of rebuilding of the hydrogen-bonded network. Because of the slow kinetics of the reformation of the hydrogen-bonded amide–amide network on cooling, the recovery of the emission energy follows a logarithmic time dependence reflecting hierarchically constrained dynamics.

The investigation that followed this work aimed basically at lowering the order/disorder phase transition temperature of m-A(14) to yield materials mechanically more resistant to

consecutive heating/cooling cycles. Several methodologies were adopted to reach this purpose: (1) changing the chemical architecture of the precursor molecule through the variation of the length of the pendant alkyl chain⁴⁰ or the nature of the cross-link;⁴¹ (2) using different synthesis conditions;^{40,41} (3) doping m-A(14) with different guest species.^{42,43}

To assess the consequences originating from the incorporation of a trivalent salt into the mono-amidosil framework, two families of m-A(14)- and m-A(8)-based hybrids incorporating a wide range of concentrations of europium triflate ($\text{Eu}(\text{CF}_3\text{SO}_3)_3$) were first investigated.⁴² In the present work, we have enlarged this study by doping m-A(14) with mono- and divalent salts (potassium triflate (KCF_3SO_3) and magnesium triflate ($\text{Mg}(\text{CF}_3\text{SO}_3)_2$, respectively) with the primary goal of getting insight into the influence of the charge density (charge/ionic radius) of the three cations and of the counteranion concentration on the structure and morphology of the mono-amidosil materials. New data concerning the m-A(14)-based mono-amidosils doped with $\text{Eu}(\text{CF}_3\text{SO}_3)_3$ not reported previously have been obtained in parallel. To probe the local coordinating environment of the alkaline and alkaline-earth metal cations in the m-A(14) medium, we have examined the cation/cross-link and cation/anion interactions. Particular attention has been paid to the impact of the three triflate salts on the order/disorder phase transition of m-A(14).

■ EXPERIMENTAL SECTION

Materials. Ethanol ($\text{CH}_3\text{CH}_2\text{OH}$, Merck, 99.8%), pyridine (py, Aldrich, 99.8%) and tetrahydrofuran (THF, 99.9%, Aldrich-Sigma) were stored over molecular sieves. Amberlyst A-21 Ion-Exchange Resin free base (Aldrich, 4.7 mequiv/g) was washed with THF and stored in an air oven at 80 °C. Palmitoyl chloride ($\text{ClC}(=\text{O})(\text{CH}_2)_{14}\text{CH}_3$, PC, Aldrich, 98%), 3-(aminopropyl)triethoxysilane ($((\text{CH}_3\text{CH}_2\text{O})_3\text{Si}(\text{CH}_2)_3\text{NH}_2$, APTES, Aldrich, 99%), potassium triflate (KCF_3SO_3 , Aldrich, 98%), and magnesium triflate ($\text{Mg}(\text{CF}_3\text{SO}_3)_2$, Aldrich, 97%) were used as received. We note that, although the correct formula of the latter salt was found to be $[\text{Mg}(\text{CF}_3\text{SO}_3)_2(\text{H}_2\text{O})]\cdot 4\text{H}_2\text{O}$,⁴⁴ for the sake of simplicity, this compound will be designated as $\text{Mg}(\text{CF}_3\text{SO}_3)_2$ throughout this work. High purity deionized water (H_2O) (type II pure water, using an Elix Reference Water Purification System 10 from Millipore) was used in all experiments.

Synthesis. The m-A(14) mono-amidosil was prepared according to the method described in detail elsewhere.^{38,39} The first stage of the synthesis procedure involved the formation of an amide cross-link between the $-\text{Cl}$ group of PC and the NH_2 group of APTES in the presence of THF, py, and Amberlyst A-21 Ion-Exchange Resin to yield the organic/inorganic hybrid precursor designated as mono-amidepropyl-triethoxysilane ($((\text{CH}_3\text{CH}_2\text{O})_3-\text{Si}-(\text{CH}_2)_3-\text{NH}-\text{C}(=\text{O})-(\text{CH}_2)_{14}-\text{CH}_3$, m-ADPTES(14)) (molar proportion, APTES:PC:Amberlyst resin:Py = 1:1:1.2:0.2) (Scheme S1 and Table S1 in the Supporting Information). The resulting solution was stirred for 1 day at room temperature. The grafting process was infrared monitored: the intensity of the band attributed to the stretching vibration of the $\text{C}=\text{O}$ group of the chloride acid, located at 1796 cm^{-1} in the spectrum of PC, was progressively reduced, and in parallel, a series of new bands appeared in the $1760\text{--}1530\text{ cm}^{-1}$ spectral interval, associated with the vibrations characteristic of the amide group. In the second stage of the synthesis procedure, a mixture of $\text{CH}_3\text{CH}_2\text{OH}$ and H_2O ($\text{Si}:\text{CH}_3\text{CH}_2\text{OH}:\text{H}_2\text{O} = 1:4:1.5$) was

added to m-ADPTES(14) to promote the hydrolysis and condensation reactions characteristic of the sol–gel process, followed by the incorporation of appropriate amounts of KCF_3SO_3 and $\text{Mg}(\text{CF}_3\text{SO}_3)_2$ (Scheme S1 in the Supporting Information). The resulting mixture was stirred in a sealed flask for 30 min and then cast to a Teflon mold, which was covered with Parafilm and left in a fume cupboard for 24 h. The white solids formed were then transferred to an air oven at 50 °C and subsequently aged for a period of 1 week. Samples m-A(14)_nY(CF₃SO₃)_x with Y = K ($x = 1$) and Mg ($x = 2$) and $\infty > n \geq 5$ (where n is the molar ratio of amide C=O groups per cation) were prepared. Further details of the synthesis procedure are collected in Table S1 in the Supporting Information.

Physical Measurements and Characterization. Nuclear Magnetic Resonance Spectroscopy. Solid-state ^{29}Si magic angle spinning (MAS) and ^{13}C cross-polarization (CP)/MAS nuclear magnetic resonance (NMR) spectra were recorded on a Bruker Avance 400 (9.4 T) spectrometer at 79.49 and 100.62 MHz, respectively. ^{29}Si MAS NMR spectra were recorded with 2 μs ($\theta \approx 30^\circ$) rf pulses, with a recycle delay of 60 s, and at a 5.0 kHz spinning rate. ^{13}C CP/MAS NMR spectra were recorded with 4 μs ^1H 90° pulse, 2 ms contact time, and a recycle delay of 4 s and at a spinning rate of 8 kHz. Chemical shifts (δ) are quoted in ppm from tetramethylsilane (TMS).

X-ray Diffraction (XRD). The XRD patterns were recorded at room temperature with a Rigaku Geigerflex D/max-c diffractometer system using monochromatic Cu K α radiation ($\lambda = 1.54 \text{ \AA}$) over the 2θ range between 4 and 80 ° at a resolution of 0.05 °. The samples were analyzed as powders and were not submitted to any thermal pretreatment.

Scanning Electron Microscopy (SEM). The SEM images were obtained at 20 kV and low vacuum on a Hitachi Field Emission S-2700 microscope. Prior to being analyzed, each sample was coated with gold. Elemental analyses on microscopic sections of selected samples were performed by energy dispersive spectroscopy (EDS).

Differential Scanning Calorimetry (DSC). The DSC measurements were obtained in a DSC131 Setaram DSC. A mass of approximately 10 mg was placed in 40 μL aluminum cans and stored in a desiccator over phosphorus pentoxide for 1 week at room temperature under vacuum. After the drying treatment, the cans were hermetically sealed and the thermograms were recorded. Each sample was heated from 20 to 250 °C at 10 °C min^{−1}. The purge gas used in all experiments was purity nitrogen (N₂) supplied at a constant 35 cm³ min^{−1} flow rate.

Thermogravimetric Analysis (TGA). Samples for thermogravimetric analysis (TGA) were transferred to open platinum crucibles and analyzed using a Q50 TA thermogravimetric analyzer at a heating rate of 10 °C min^{−1} with dried N₂ as purging gas (flow rates of 40 and 60 cm³ min^{−1} in the balance and in the sample, respectively).

Fourier Transform Infrared (FT-IR). The FT-IR spectra were acquired at room temperature using a Bruker 22 (Vektor) spectrometer placed inside a glovebox with a dry argon atmosphere. The spectra were collected over the 4000–400 cm^{−1} range by averaging 150 scans at a resolution of 2 cm^{−1}. Solid samples (2 mg) were finely ground, mixed with approximately 175 mg of dried potassium bromide (Merck, spectroscopic grade), and pressed into pellets. FT-IR/ATR spectra recorded as function of temperature were obtained with a SPECAC temperature controller in a ATR configuration

using a High Temperature Golden Gate™ MkII ATR Accessory. The spectra were collected between room temperature and 120 °C in the 4000–500 cm^{−1} range by averaging 64 scans at a resolution of 1 cm^{−1}.

To evaluate complex band FT-IR envelopes and to identify underlying spectral components, the iterative least-squares curve-fitting procedure in the PeakFit⁴⁵ software was used extensively throughout this study. The best fit of the experimental data was obtained by varying the frequency, bandwidth, and intensity of the bands. Taking into account the morphology of materials under investigation, we decided to employ Voigt band shapes. A linear baseline correction with a tolerance of 0.2% was employed. The standard errors of the curve-fitting procedure were less than 0.03.

RESULTS AND DISCUSSION

Structure. The ^{13}C CP/MAS NMR spectra of the m-A(14)-based mono-amidosils doped with KCF_3SO_3 and $\text{Mg}(\text{CF}_3\text{SO}_3)_2$ (parts a and b of Figure S1 in the Supporting Information, respectively) have been used to characterize the structure and the conformational order of the alkyl chains. The position δ and assignment^{27–34,38,39} of the resonance peaks of the ^{13}C CP/MAS of these materials and analogues are summarized in Table 1.

The ^{13}C CP/MAS NMR spectra of the K⁺- and Mg²⁺-doped m-A(14)-based mono-amidosils are dominated by a peak centered around 33 ppm (parts a and b of Figure S1 in the

Table 1. ^{13}C CP/MAS NMR Data of Selected m-A(14)_nKCF₃SO₃ and m-A(14)_nMg(CF₃SO₃)₂ Mono-Amidosils and ^{29}Si MAS NMR Data of the m-A(14)_nKCF₃SO₃, m-A(14)_nMg(CF₃SO₃)₂, and m-A(14)_nEu(CF₃SO₃)₃⁴² Mono-Amidosils^a

^{13}C CP/MAS NMR						
m-A(14) _n Y(CF ₃ SO ₃) _x						
Y ^{z+}		K ⁺		Mg ²⁺		
n	∞	5	100	10	5	attribution ^{27–34,38,39}
	174	173	173	175	174	C ¹²
	42	43	43	42	42	C ³
	36	36	36	36	36	C ⁶
	34	34	34	34	34	C ⁹
	32	33	33	33	33	C ^{8 trans}
		30, sh	30, sh	30	30	C ^{8 gauche}
	26	26	26	26	26	C ⁷
	24	24	24	24/23	24/23	C ² /C ¹⁰
	14	14	14	14	14	C ¹¹
	11	10		10	10	C ¹
^{29}Si MAS NMR						
m-A(14) _n Y(CF ₃ SO ₃) _x						
Y ^{z+}	n	T ¹	T ²	T ³	c	empirical formula
	∞	−49.5	−57.8	−67.0	74	R'Si(OSi) _{0.8} (OH) _{1.1}
K ⁺	5	−48.0	−58.5	−67.1	78	R'Si(OSi) _{1.2} (OH) _{0.7}
Mg ²⁺	100	−47.8	−58.2	−66.8	76	R'Si(OSi) _{1.1} (OH) _{0.7}
	10	−49.8	−59.9	65.0	81	R'Si(OSi) _{1.2} (OH) _{0.6}
Eu ³⁺	200	−47.8	58.1	66.9	77	R'Si(OSi) _{1.1} (OH) _{0.7}
	10	−50.0	60.0	65.8	83	R'Si(OSi) _{1.2} (OH) _{0.5}

^a δ are given in ppm. Notes: T¹ (R'—Si(OSi)(OH)₂); T² (R'—Si(OSi)₂(OH)); T³ (R'—Si(OSi)₃); c (polycondensation degree) = 1/3(%T¹ + 2%T² + 3%T³) × 100; R' = CH₃(CH₂)₁₄C(=O)NH—(CH₂)₃—.

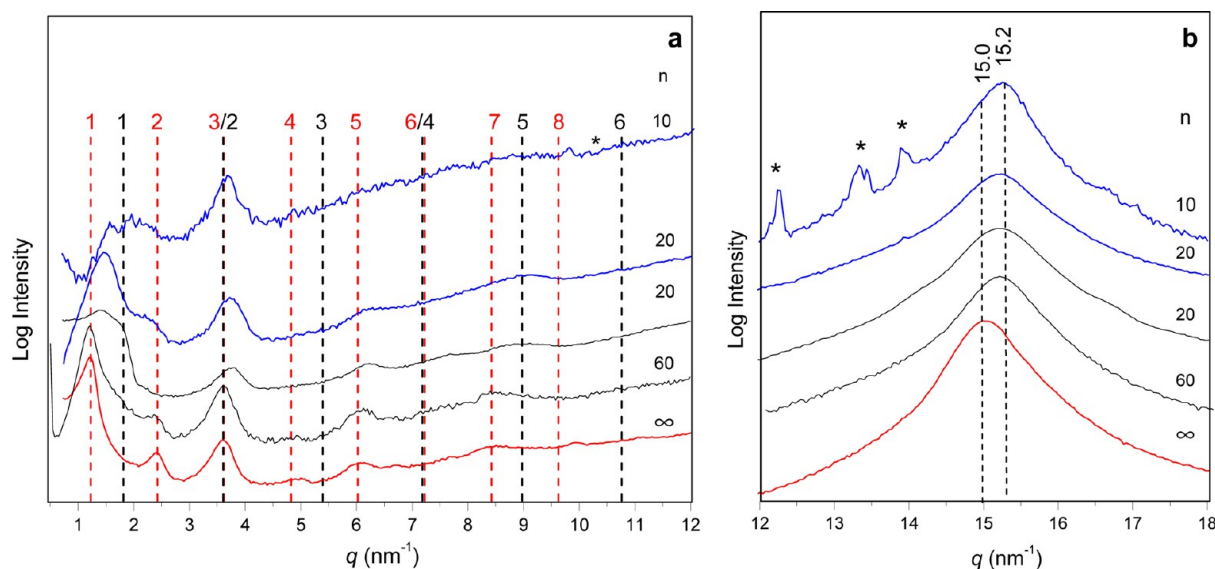


Figure 1. XRD patterns of m-A(14)^{38,39} (red line), m-A(14)_nKCF₃SO₃ (black line), and m-A(14)_nMg(CF₃SO₃)₂ (blue line) mono-amidosils in the low- (a) and high-*q* (b) range. The vertical dashed lines in part a indicate the *k*th orders of the two lamellar structures found.

Supporting Information, respectively) attributed to the resonance of the C⁸ carbon atoms of the alkyl chains (Scheme S1 in the Supporting Information and Table 1) and characteristic of the alkyl chains all-*trans* zigzag conformations.^{38,39,46,47} This means that in the samples studied most of the alkyl chains are densely packed and adopt all-*trans* conformations. The shoulder discerned at 30 ppm in the spectra of m-A(14)₅KCF₃SO₃ and m-A(14)₁₀₀Mg(CF₃SO₃)₂ (parts a and b of Figure S1 in the Supporting Information, respectively, and Table 1) indicate that only a minor population of the alkyl chains adopt *gauche* conformations in these samples.⁴⁶ In the m-A(14)_nMg(CF₃SO₃)₂ materials with *n* = 10 and 5, the distinct and sharp peak which develops at 30 ppm (Figure S1b in the Supporting Information and Table 1) demonstrates that in both Mg(CF₃SO₃)₂-doped mono-amidosils the relative proportion of *gauche* conformers is higher. The peaks associated with the resonance of the carbon atoms of the alkyl chains, of the Si-bonded propyl chains, and of the amide carbonyl groups are also detected (Figure S1a and b and Scheme S1 in the Supporting Information and Table 1). Comparison of these data with those reported for m-ADPTES(14)^{38,39} reveals that no cleavage of the functional groups of the precursor molecule occurred during the second stage of the synthesis procedure. The ¹³C CP/MAS results also demonstrate that the hydrolysis reaction was complete in all the doped m-A(14) mono-amidosils analyzed (Figure S1a and b and Scheme S1 in the Supporting Information and Table 1), as indicated by the absence of the peaks associated with the resonance of the ethoxyl carbon atoms (C⁴ and C⁵).^{38,39}

The ²⁹Si MAS NMR spectra of the K⁺- and Mg²⁺-doped mono-amidosils display two medium intensity signals at ca. −58 and −66 ppm (parts a and b of Figure S2 in the Supporting Information, respectively), assigned to T² and T³ substructures, respectively (Table 1). The T¹ signal appears as a shoulder. The absence of T⁰ and Q-type signals in these spectra confirms the complete conversion of the precursor and the preservation of the Si–C bonds, respectively. The condensation degrees *c* deduced for m-A(14)₅KCF₃SO₃ (78%) and m-A(14)₁₀₀Mg(CF₃SO₃)₂ (76%) practically coincide with that calculated for the non-doped m-A(14) matrix (74%)^{38,39} and

for the dilute sample m-A(14)₂₀₀Eu(CF₃SO₃)₃ (77%)⁴² (Table 1). These results strongly suggest the formation of a 2D siloxane network in the m-A(14)₅KCF₃SO₃ and m-A(14)₁₀₀Mg(CF₃SO₃)₂ hybrid materials, a situation similar to that found in m-A(14)₂₀₀Eu(CF₃SO₃)₃.⁴² In the case of the more concentrated m-A(14)₁₀Mg(CF₃SO₃)₂ and m-A(14)₁₀Eu(CF₃SO₃)₃ samples, slightly higher *c* values were found (81 and 83,⁴² respectively) (Table 1). The empirical formulas derived for K⁺-, Mg²⁺-, and Eu³⁺-doped m-A(14) samples show that some hydroxyl groups persisted bonded to the silicon atoms (Table 1).

The XRD patterns of selected K⁺- and Mg²⁺-doped m-A(14)-based mono-amidosils in the 0.5–12 and 12–18 nm^{−1} *q* (where *q* = 4π sin *θ*/λ, with *θ* and λ being half of the scattering angle and the wavelength, respectively) ranges are represented in parts a and b of Figure 1, respectively.

In the low *q* range, these XRD patterns exhibit a series of peaks (Figure 1a). In the pattern of the dilute m-A(14)₆₀KCF₃SO₃ material, the peak discerned at *q* = 1.20 nm^{−1} corresponds to the first order of the *k*th reflections of a lamellar structure with spacing *d*₁ = 5.20 nm (where *d* = *k*2π/*qk*) (red vertical dotted lines in Figure 1a). The latter value coincides with the interlamellar distance reported for m-A(14) (5.0 ± 0.2 nm),^{38,39} thus confirming the presence of the lamellar bilayer structure of the m-A(14) framework in this doped sample. The presence of a shoulder at *q* = 1.79 nm^{−1}, more visible in the high *q* range side of the first peak of the mono-amidosil with higher content of KCF₃SO₃ (*n* = 20) (Figure 1a), strongly suggests that at both compositions the original lamellar arrangement of m-A(14) coexists with a new lamellar structure with lower interlamellar spacing (*d*₂ = 3.50 nm) (black vertical dotted lines in Figure 1a). The reduction of the interlamellar spacing of the new phase with respect to the original one was also reported for the mono-amidosils doped with Eu(CF₃SO₃)₃, although the effect was not so marked (*d*₂ = 4.47 nm).⁴² The m-A(14)₂₀Mg(CF₃SO₃)₂ sample gives rise to a prominent peak at *q* = 1.44 nm^{−1}. Although the shoulder centered near 2.33 nm^{−1} and the peak at 3.71 nm^{−1} seem to indicate the presence of the lamellar structure of m-A(14) and the shape of the 1.44 nm^{−1} peak suggests the existence of a

second lamellar phase (Figure 1a), any conclusions are subject to much uncertainty without complementary data (e.g., small angle X-ray scattering (SAXS) data). At higher $\text{Mg}(\text{CF}_3\text{SO}_3)_2$ content ($n = 10$), the XRD pattern in the $0.5\text{--}2\text{ nm}^{-1}$ q range becomes considerably less well resolved, making its interpretation even more speculative. We will revisit these aspects below in the context of the discussion of the DSC results. The lack of SAXS data prevents us from estimating the coherence length of the lamellar order of the $\text{m-A}(14)_n\text{KCF}_3\text{SO}_3$ and $\text{m-A}(14)_n\text{Mg}(\text{CF}_3\text{SO}_3)_2$ mono-amidosils.

In the high q range of the XRD patterns of the $\text{m-A}(14)_n\text{KCF}_3\text{SO}_3$ and $\text{m-A}(14)_n\text{Mg}(\text{CF}_3\text{SO}_3)_2$ samples selected (Figure 1b), the most prominent event is a broad, non-resolved band centered at $q = 15.2\text{ nm}^{-1}$. This peak, which receives the contribution of the order within the siliceous domains,⁴⁸ as well as amide–amide¹⁹ and chain–chain⁴⁹ spacings, is upshifted with respect to that produced by the non-doped $\text{m-A}(14)$ matrix at $q = 15.0\text{ nm}^{-1}$ (Figure 1b).

Finally, we must point out that in the XRD pattern of $\text{m-A}(14)_{10}\text{Mg}(\text{CF}_3\text{SO}_3)_2$ new peaks (marked with asterisks in Figure 1) emerge, denoting the formation of free, crystalline $\text{Mg}(\text{CF}_3\text{SO}_3)_2$ at this composition.

The XRD findings lead us to conclude that the addition of guest ionic species of distinct nature (i.e., the triflate salts KCF_3SO_3 , $\text{Mg}(\text{CF}_3\text{SO}_3)_2$, and $\text{Eu}(\text{CF}_3\text{SO}_3)_3$ ⁴²) to $\text{m-A}(14)$ promoted the formation of new lamellar phases with lower interlamellar spacing than that of the original structure of $\text{m-A}(14)$. In all the cases examined, the latter phase persists independently of the type and concentration of dopant. A very interesting fact worth emphasizing is the extraordinary encapsulating ability exhibited by the host hybrid matrix. Out of the set of mono-amidosils analyzed by XRD, evidence of the formation of pure crystalline guest salt was only found in the case of the salt-rich $\text{m-A}(14)_{10}\text{Mg}(\text{CF}_3\text{SO}_3)_2$ sample, a situation which was also reported for the analogue $\text{m-A}(14)_{10}\text{Eu}(\text{CF}_3\text{SO}_3)_3$.⁴² In all the other samples studied, the crystallization of the guest monovalent, divalent, and trivalent triflate salts was entirely suppressed (cf. XRD patterns reproduced in Figure S3a in the Supporting Information). The guest salt crystallization tendency of the more concentrated mono-amidosils $\text{m-A}(14)_5\text{KCF}_3\text{SO}_3$ and $\text{m-A}(14)_5\text{Mg}(\text{CF}_3\text{SO}_3)_2$ will be discussed below.

Morphology. The SEM images of $\text{m-A}(14)_{20}\text{KCF}_3\text{SO}_3$ and $\text{m-A}(14)_5\text{KCF}_3\text{SO}_3$ reveal a texture composed of micrometric plates organized in a way that mimics the very tight arrangement of cabbage leaves (Figure 2a/b and c/d, respectively). The packing of the plates in the $\text{m-A}(14)_n\text{Mg}(\text{CF}_3\text{SO}_3)_2$ samples with $n = 100, 10$, and 5 is considerably less dense (Figure 2e/f, g/h, and i/j, respectively) than that in the K^+ -doped mono-amidosils. In the $\text{Mg}(\text{CF}_3\text{SO}_3)_2$ -doped materials, plates with nanometer thickness stack regularly along a sort of tile-to-tile piling (Figure 2f) that yields a microstructure which is close to the characteristic lamellar stacking of foliated schist (Figure 2e/g/i). The $\text{m-A}(14)_{60}\text{Eu}(\text{CF}_3\text{SO}_3)_3$ sample exhibits a sea-sponge-like morphology (Figure 2k), consisting of very thin, folded films assembled along an edge-to-face fashion. The void-like structure of this sample is clearly evident at higher magnification (Figure 2l). Figure 2m shows that in $\text{m-A}(14)_{20}\text{Eu}(\text{CF}_3\text{SO}_3)_3$ the tight arrangement of the films results in the formation of dense aggregates of ca. $10\text{ }\mu\text{m}$ diameter spherical objects. The analysis of Figure 2n allows concluding that the substructure of these entities closely resembles that of $\text{m-A}(14)_{60}\text{Eu}(\text{CF}_3\text{SO}_3)_3$

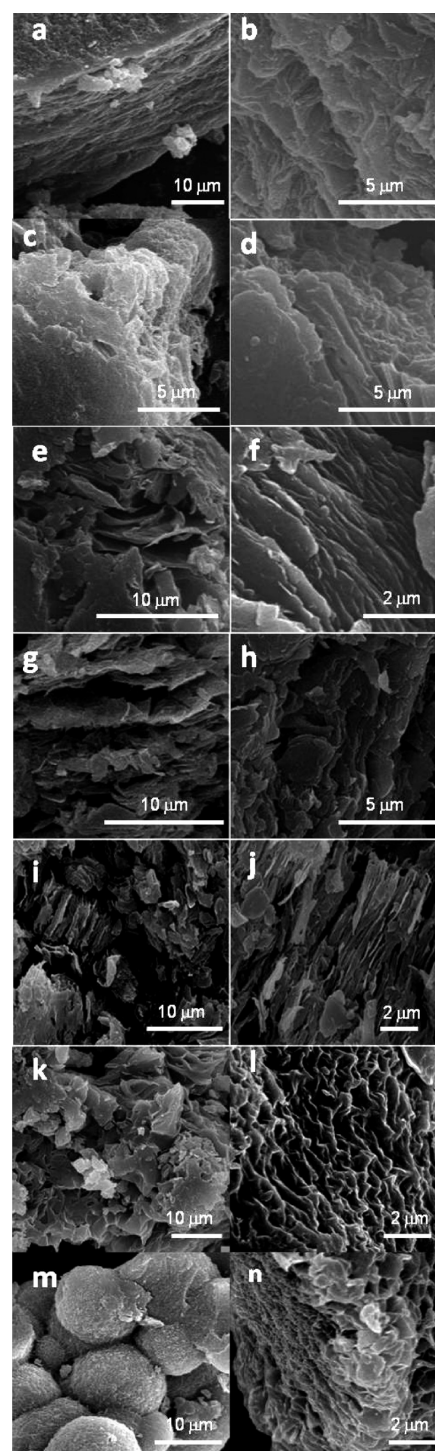


Figure 2. SEM images of $\text{m-A}(14)_{20}\text{KCF}_3\text{SO}_3$ (a and b), $\text{m-A}(14)_5\text{KCF}_3\text{SO}_3$ (c and d), $\text{m-A}(14)_{100}\text{Mg}(\text{CF}_3\text{SO}_3)_2$ (e and f), $\text{m-A}(14)_{10}\text{Mg}(\text{CF}_3\text{SO}_3)_2$ (g and h), $\text{m-A}(14)_5\text{Mg}(\text{CF}_3\text{SO}_3)_2$ (i and j), $\text{m-A}(14)_{60}\text{Eu}(\text{CF}_3\text{SO}_3)_3$ (k and l), and $\text{m-A}(14)_{20}\text{Eu}(\text{CF}_3\text{SO}_3)_3$ (m and n) mono-amidosils.

(Figure 2l). X-ray mapping of a zoom area of the salt-rich $\text{m-A}(14)_{20}\text{KCF}_3\text{SO}_3$ (Figure 3a), $\text{m-A}(14)_{10}\text{Mg}(\text{CF}_3\text{SO}_3)_2$ (Figure 3d), and $\text{m-A}(14)_5\text{Eu}(\text{CF}_3\text{SO}_3)_3$ (Figure 3g) mono-amidosils showed that, as expected, the Si atoms are found all over the surface of the plates (Figure 3b, e, and h, respectively), whereas the K^+ ions (Figure 3c) and the Eu^{3+} ions (Figure 3i) are confined within certain regions of the material, being

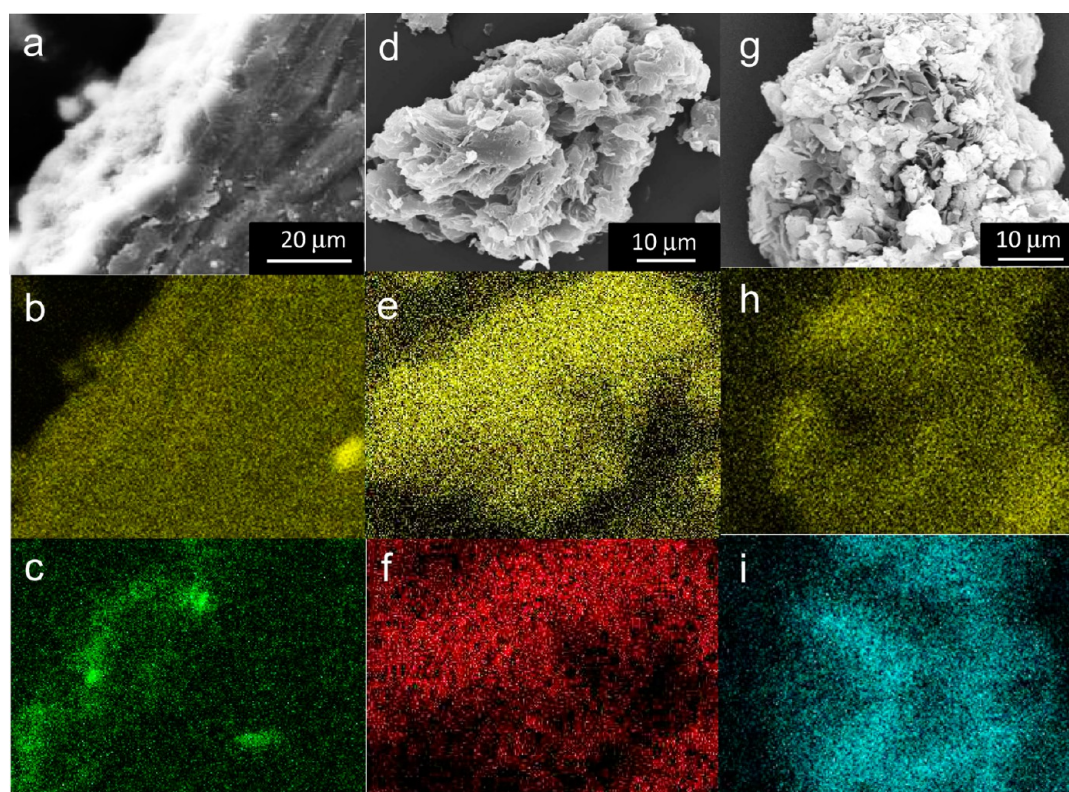


Figure 3. SEM images of the $m\text{-A}(14)_{20}\text{KCF}_3\text{SO}_3$ (a), $m\text{-A}(14)_{10}\text{Mg}(\text{CF}_3\text{SO}_3)_2$ (d), and $m\text{-A}(14)_5\text{Eu}(\text{CF}_3\text{SO}_3)$ (g) mono-amidosils and corresponding EDS mapping for Si (b, e, and h, respectively), K (c), Mg (f), and Eu (i).

presumably anchored to the amide cross-links and also possibly to the residual silanol groups. The latter finding is interesting, considering that in $m\text{-A}(14)_5\text{Eu}(\text{CF}_3\text{SO}_3)$ the host hybrid matrix is no longer able to accommodate all the salt incorporated and as a consequence part of it is expelled.

Thermal Behavior. To further characterize the K^+ - and Mg^{2+} -doped mono-amidosils, DSC and TGA measurements were performed.

When dealing with alkyl/siloxane hybrid materials, DSC is a particularly useful technique, providing rich information about the energetics of the order/disorder phase transition of the alkyl chains. The enthalpy change (ΔH) observed during fusion of alkyl chains is associated with a large cohesive van der Waals energy term, whereas the entropy change (ΔS) involves a conformational term, an excluded volume term, and a dominating volume expansion term.⁵⁰

The DSC curves of the $m\text{-A}(14)_n\text{KCF}_3\text{SO}_3$ and $m\text{-A}(14)_n\text{Mg}(\text{CF}_3\text{SO}_3)_2$ mono-amidosils in the 20–250 °C range are represented in parts a and b of Figure 4, respectively. The DSC curves of KCF_3SO_3 and $\text{Mg}(\text{CF}_3\text{SO}_3)_2$ between 25 and 300 °C are found in Figure S3b in the Supporting Information.

In the DSC curves of the K^+ -containing samples with $n = 60$, 20, and 5, two endothermic events are visible independently of salt composition: a distinct peak centered at ca. 91 °C and a broad peak centered at approximately 40 °C (Figure 4a and Table 2). On the basis of the conclusions retrieved from XRD data and on the values of ΔH and ΔS , these two endotherms are ascribed to the order/disorder phase transition of the lamellar structure of the $m\text{-A}(14)$ matrix and of the new phase which is formed in the presence of KCF_3SO_3 , respectively. The same situation is encountered in the Mg^{2+} -doped mono-

amidosils with $n = 100$ and 20, the DSC curves of which also exhibit two endothermic features at 95 and 40 °C (sharp) (Figure 4b and Table 2). In contrast, the salt-rich $m\text{-A}(14)_{10}\text{Mg}(\text{CF}_3\text{SO}_3)_2$ and $m\text{-A}(14)_5\text{Mg}(\text{CF}_3\text{SO}_3)_2$ samples give rise to a single endothermic peak, sharp and intense, at 40 °C, whereas the peak associated with the occurrence of non-doped $m\text{-A}(14)$, expected around 95 °C (Figure 4a), is no longer seen (Figure 4b and Table 2).

The thermal stability of hybrid materials can be of crucial importance in determining the suitability of certain materials for specific applications. The TGA curves of selected K^+ - and Mg^{2+} -doped $m\text{-A}(14)$ -based mono-amidosils are shown in parts a and b of Figure S4 in the Supporting Information, respectively. The most remarkable aspect of these curves is the striking coincidence demonstrated by the TGA curves of $m\text{-A}(14)_{60}\text{KCF}_3\text{SO}_3$ and $m\text{-A}(14)$ (Figure S4a in the Supporting Information). In both samples, thermal decomposition begins around 200 °C and takes place in a single stage characterized by a transition temperature of 444 °C and a weight loss of approximately 80%. In contrast, the degradation of $m\text{-A}(14)_{20}\text{KCF}_3\text{SO}_3$ and $m\text{-A}(14)_{100}\text{Mg}(\text{CF}_3\text{SO}_3)_2$ is a two-step process (see derivative curves of parts a and b of Figure S4 in the Supporting Information, respectively). The decomposition of the two materials is initiated around 150 and 200 °C, respectively (weight loss $\approx 12\%$ and a transition temperature of about 257 °C). The second decomposition takes place at 400 and 350 °C for $m\text{-A}(14)_{20}\text{KCF}_3\text{SO}_3$ and $m\text{-A}(14)_{100}\text{Mg}(\text{CF}_3\text{SO}_3)_2$, respectively (characteristic transition temperatures of 414 and 439 °C, respectively) and a global weight loss of ca. 65%. The thermal behavior of the salt-rich $m\text{-A}(14)_5\text{Mg}(\text{CF}_3\text{SO}_3)_2$ mono-amidosil differs markedly from those of the previous samples, since it is manifested in three different stages

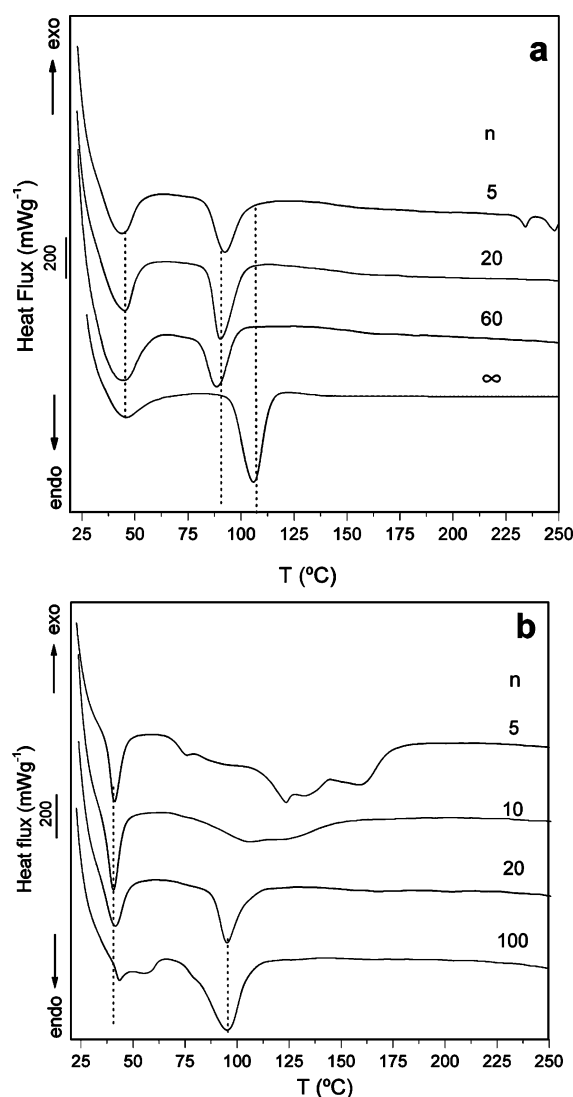


Figure 4. DSC curves of m-A(14)^{38,39} (a) and of the m-A(14)_nKCF₃SO₃ (a) and m-A(14)_nMg(CF₃SO₃)₂ (b) mono-amidosils.

(Figure S4b in the Supporting Information). This compound starts to suffer decomposition at about 50 °C. The slight weight loss (≈5%) (characteristic transition temperature of 82 °C) that follows is most likely associated with the release of water molecules entrapped within the material due to the presence of the very hygroscopic magnesium salt, as discussed below. At temperatures higher than approximately 230 °C, two regions corresponding to weight losses of ~55 and 20%, respectively, and characteristic temperatures of 414 and 477 °C, respectively, are discerned in the TGA curve of this sample. In all the mono-amidosil samples, ca. 20% of the mass remains to be decomposed at 700 °C (Figure S4a and S4b in the Supporting Information). The weight losses detected between 150 and 200 °C are most likely related to the release of water molecules formed through the condensation of silanol (Si–OH) groups. The weight loss taking place above 300 °C is attributed to the degradation of the alkyl chains, which ends up with a stable (Si–O–Si)-based residue.

These results lead us to conclude that doping m-A(14) with low contents of KCF₃SO₃ and Mg(CF₃SO₃)₂ did not influence the thermal stability of the hybrid matrix. In the case of the m-A(14)₂₀KCF₃SO₃ and m-A(14)₅Mg(CF₃SO₃)₂ samples, the salt

Table 2. DSC Data of m-A(14)^{38,39} and of the m-A(14)_nKCF₃SO₃, m-A(14)_nMg(CF₃SO₃)₂, and m-A(14)_nEu(CF₃SO₃)₃⁴² Mono-Amidosils^a

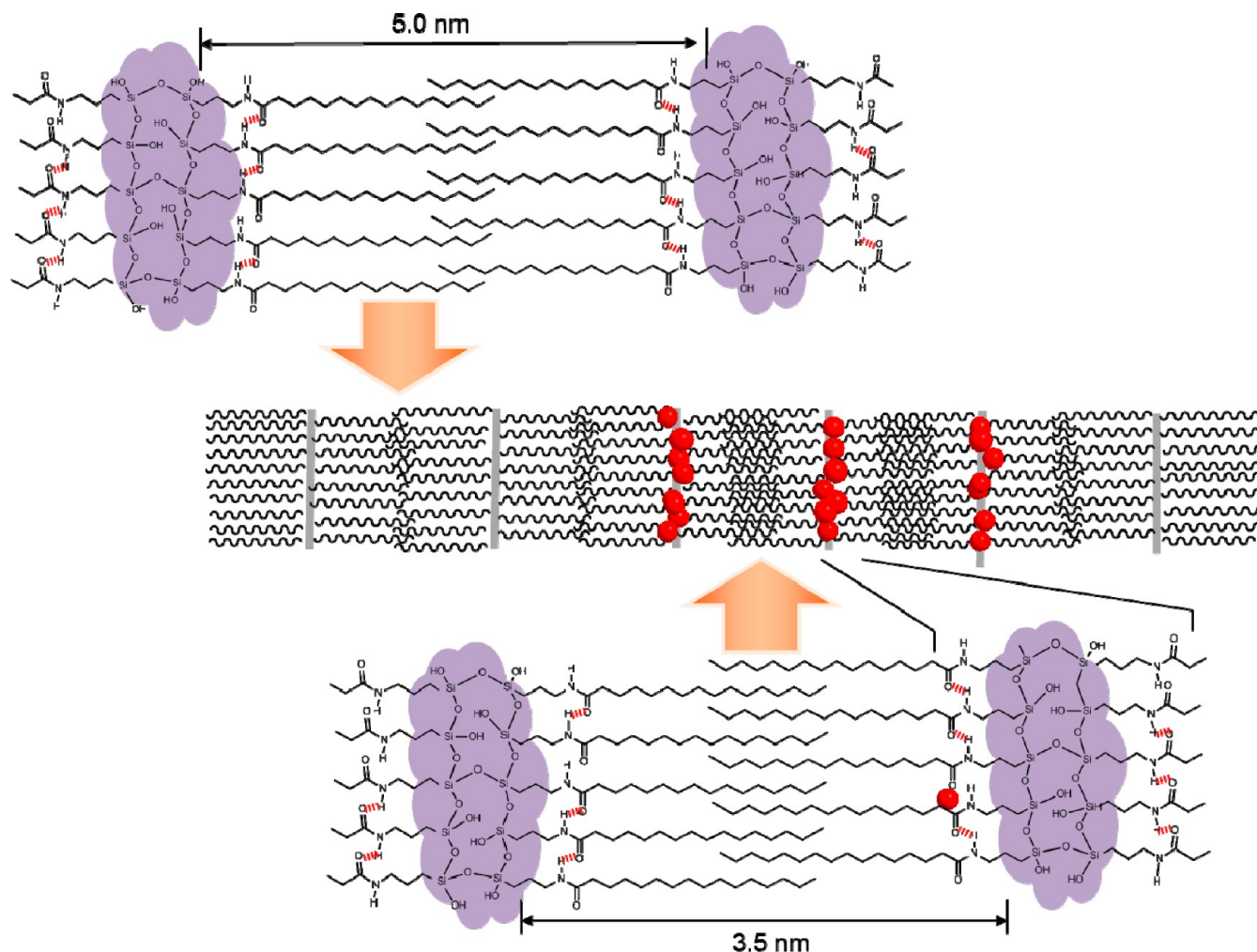
m-A(14) _n M(CF ₃ SO ₃) _x						
M ²⁺	n	T _{onset} (°C)	T _{peak} (°C)	fwhm (°C)	ΔH (J g ⁻¹)	ΔS (J g ⁻¹ °C)
K ⁺	∞	96	106	10.61	30.44	0.287
	60	78	89	9.63	18.4	0.21
	20	79	92	9.88	24.7	0.27
			40			
	5		247			
			234			
Mg ²⁺	100	70	93	11.6	20.3	0.22
			40			
			95	13.1		0.31
			40			
	20	79	95	11.1	23.0	0.24
			40			
	10		40			
	5		132			
Eu ³⁺	200	100	123			
			40			
			97			
			73			
	60	82	99			
			94			

^afwhm = full width at half-maximum.

exerted a destabilizing effect. Another interesting aspect worth mentioning is the fact that the addition of Mg(CF₃SO₃)₂ (in reality [Mg(CF₃SO₃)₂(H₂O)]·4H₂O, see the Experimental Section and Figure S3c in the Supporting Information) to m-A(14) was clearly beneficial from the standpoint of hygroscopicity, since we have demonstrated that m-A(14)₁₀₀Mg(CF₃SO₃)₂ is completely anhydrous and m-A(14)₅Mg(CF₃SO₃)₂ is only slightly hygroscopic.

Alkyl Chains Conformational Disorder. To get information on the degree of conformational disorder of the alkyl chains, the FT-IR region characteristic of the symmetric and asymmetric CH₂ stretching (ν_sCH₂ and ν_aCH₂, respectively) vibration modes was analyzed.

The ν_aCH₂ and ν_sCH₂ regions of the FT-IR spectra of the m-A(14)_nKCF₃SO₃ (*n* = 60 and 20) and m-A(14)_nMg(CF₃SO₃)₂ (*n* = 100 and 20) mono-amidosils exhibit two intense features at about 2920/2919 cm⁻¹ (medium (m), full width at half-maximum (fwhm) = 21–23 cm⁻¹) and 2850 cm⁻¹ (m, fwhm = 14 cm⁻¹) (parts a and b of Figure S5, respectively, and Table S2 in the Supporting Information). Comparison of the position, intensity, and fwhm of these bands with those produced by the m-A(14) matrix (2920 cm⁻¹ (very strong (vS), fwhm = 21 cm⁻¹) and 2850 cm⁻¹ (strong (S), fwhm = 10 cm⁻¹), respectively^{38,39}) demonstrates that in the K⁺- and Mg²⁺-doped mono-amidosils with *n* ≥ 20 the great majority of the alkyl chains adopt all-*trans* conformations, meaning that they are fully stretched and highly packed.^{51–57} Therefore, in these four mono-amidosils, the steric hindrance produced by the coordination of the K⁺ and Mg²⁺ ions to the C=O groups of the amide cross-links and to the residual Si–OH groups of the siliceous network and also by the presence of the bulky triflate

Scheme 1. Tentative Representation of the Structure of the m-A(14)₁₀₀MgCF₃SO₃ Mono-Amidosil^a

^aThe cations (red spheres) may be bonded to the oxygen atoms of the carbonyl groups of the cross-links or to the silanol groups of the siliceous network. For the sake of clarity, the anions have been omitted.

counterions located in the neighborhood of each cation for electroneutrality purposes (one and two, respectively) does not affect the degree of order of the alkyl chains, an extraordinary finding also found in the case of the m-A(14)₆₀Eu(CF₃SO₃)₃ sample.⁴² Scheme 1 represents a tentative description of the structure of the m-A(14)₁₀₀Mg(CF₃SO₃)₂ sample drawn on the basis of the conclusions retrieved from ²⁹Si MAS NMR, XRD, and FT-IR data.

Upon further incorporation of KCF₃SO₃ into m-A(14) ($n = 5$), the ν_a CH₂ and ν_s CH₂ modes underwent a shift to lower wavenumbers (2916 and 2849 cm⁻¹, respectively) (Figure S5a and Table S2 in the Supporting Information). This downshift may be interpreted as an indication that in this salt-rich sample the alkyl chains are more ordered than in m-A(14) itself. The reverse situation occurred upon increasing Mg(CF₃SO₃)₂ concentration to $n = 10$ and 5, the shift of the ν_a CH₂ and ν_s CH₂ modes being to higher wavenumbers (2924 and 2854 cm⁻¹, respectively) (Figure S5b and Table S2 in the Supporting Information). This evidence proves that in the latter two samples the relative population of alkyl chains in *gauche* conformations increased and consequently they became more disordered, confirming the conclusions drawn from the ¹³C CP/MAS NMR data discussed above. We recall that in the Eu(CF₃SO₃)₃-based mono-amidosils with $n = 20$ and 10 the

same disordering effect was reported.⁴² Thus, the structuring observed in the salt-rich m-A(14)₅KCF₃SO₃ material is indeed quite surprising. We note, however, that at this composition salting-out takes place. On account of the monovalent character of the K⁺ ion, we may speculate that the steric hindrance associated with this cation is less important than that involving the divalent Mg²⁺ and trivalent Eu³⁺ cations which need to interact with two and three triflate ions to ensure electro-neutrality, respectively.

Cation Coordination. The addition of a wide range of concentrations of KCF₃SO₃, Mg(CF₃SO₃)₂, and Eu(CF₃SO₃)₃ to m-A(14) was expected to affect to a lesser or greater extent the interactions occurring within the non-doped matrix. Chemically, the K⁺, Mg²⁺, and Eu³⁺ ions differ substantially in terms of charge density and coordination number (Table S3, Supporting Information). According to Pearson's classification, these three species are classed as hard Lewis acids, their hardness increasing in the order K⁺ ≤ Mg²⁺ < Eu³⁺.⁵⁸ Ideally, in the m-A(14) host hybrid structure, the C=O oxygen atoms of the amide cross-links are the sole coordinating sites available for guest cations. However, bonding to the oxygen atoms of residual Si—OH groups located at the siliceous network (see ²⁹Si MAS NMR data of Table 1) is also prone to occurring. Apart from interacting with the C=O and

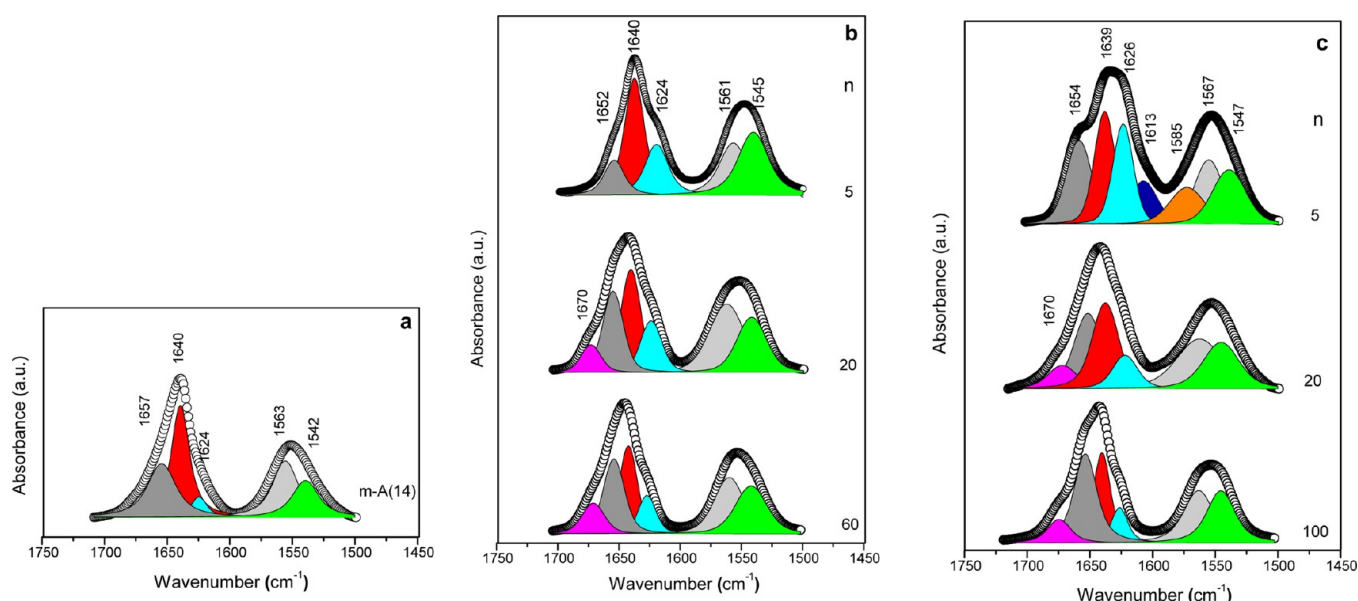


Figure 5. Curve-fitting results of the amide I and amide II regions of m-A(14)^{38,39} (a) and of selected m-A(14)_nKCF₃SO₃ (b) and m-A(14)_nMg(CF₃SO₃)₂ (c) mono-amidosils.

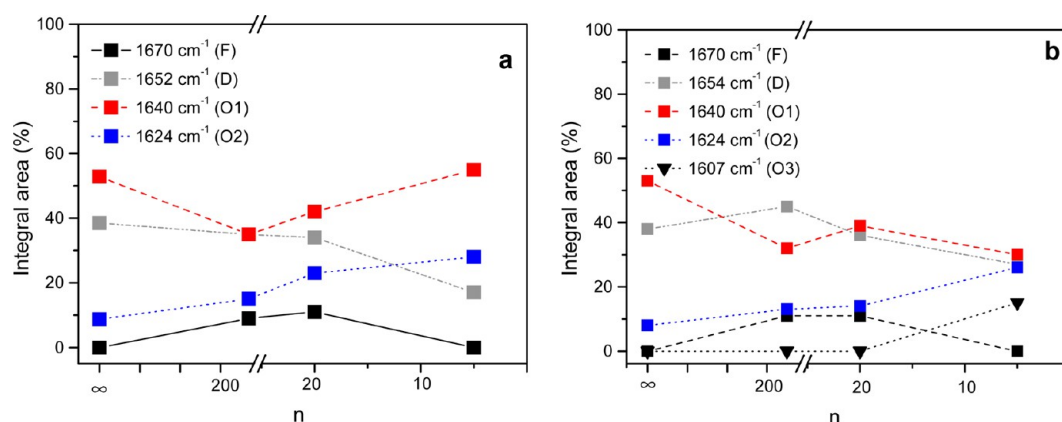


Figure 6. Composition dependence of the integral area fraction of the different spectral components resolved in the amide I region of m-A(14)^{38,39} and of the m-A(14)_nKCF₃SO₃ (a) and m-A(14)_nMg(CF₃SO₃)₂ (b) mono-amidosils.

Si—OH groups, the three cations may bond to the oxygen atoms of SO₃ end-groups of the triflate ions, especially at high salt content when ionic association is favored. At last, in the case of the very hygroscopic Mg(CF₃SO₃)₂ (Figures S3 and S4 in the Supporting Information) and Eu(CF₃SO₃)₃ salts, the presence of water molecules in the first coordination sphere is foreseeable. All of these donor species (i.e., C=O, Si—OH, CF₃SO₃[−], and H₂O) are Lewis hard bases. The cation/cross-link and cation/anion interactions will be examined as follows.

After being incorporated into the mono-amidosil framework, the K⁺ and Mg²⁺ species may either interact with “free” carbonyl (C=O) groups or coordinate to hydrogen-bonded C=O groups. In the latter case, the alkali and alkaline-earth metal ions will have to disrupt the network of hydrogen bonds formed via the amide groups throughout the salt-free m-A(14). To assess how the hydrogen-bonded array of the host m-A(14) matrix was modified by doping with KCF₃SO₃ and Mg(CF₃SO₃)₂ (both in terms of strength and distribution of the hydrogen bonds), two characteristic bands of the amide cross-links were inspected: the amide I and amide II bands.

The amide I mode,⁵⁹ which receives a major contribution of the C=O stretching vibration, is sensitive to the specificity and magnitude of hydrogen bonding. Typically, the amide I band consists of several distinct components that correspond to different environments of the C=O groups.^{60–62} The involvement of C=O groups in hydrogen bonding interactions results in a shift of the amide I band of the non-bonded C=O group to lower wavenumbers.^{60,61} The amide II mode, essentially associated with the N—H in-plane bending vibration, is sensitive to chain conformation and intermolecular hydrogen bonding, providing useful information about the distribution of hydrogen bond strengths.⁶⁰ When the C=O group is included in hydrogen-bonded aggregates, the amide II band emerges at higher wavenumber than in the case of the free C=O group.

The FT-IR spectra of the K⁺- and Mg²⁺-doped m-A(14)-based mono-amidosil hybrids in the amide I and amide II regions are reproduced in parts a and b of Figures S6 in the Supporting Information, respectively. To determine the components of the amide I and amide II envelopes of selected mono-amidosils, curve-fitting procedures were performed in the

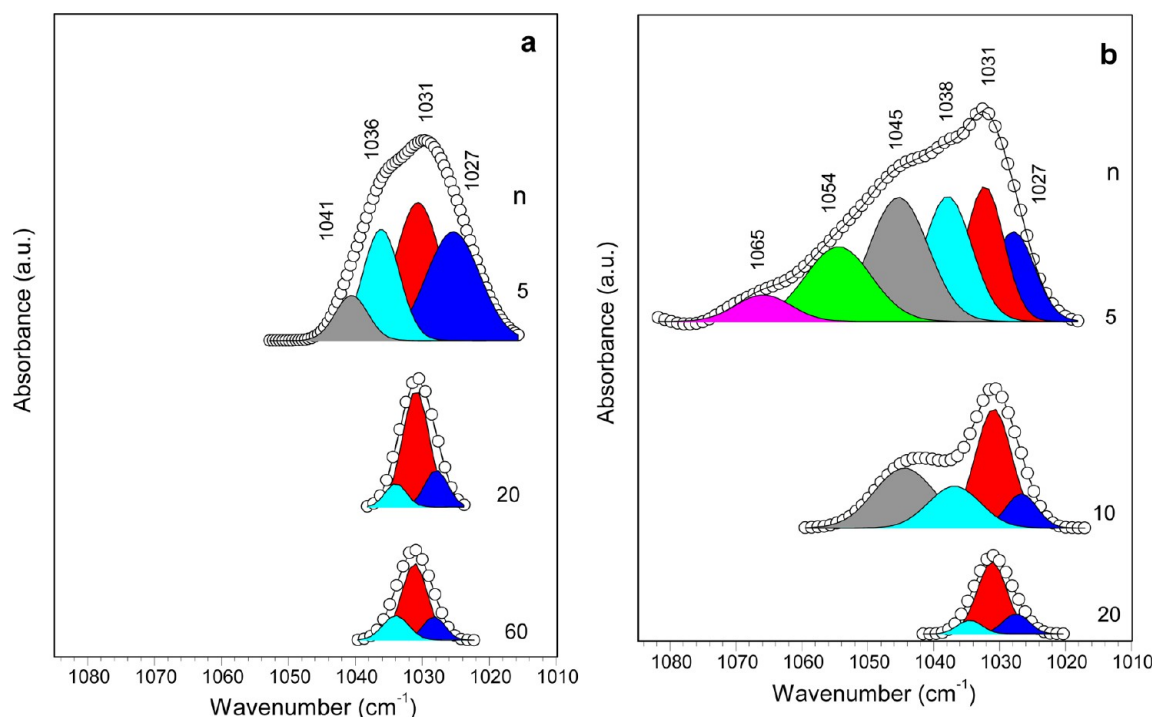


Figure 7. Curve-fitting results of the $\nu_s\text{SO}_3$ region of the FT-IR spectra of the $\text{m-A}(14)_n\text{KCF}_3\text{SO}_3$ (a) and $\text{m-A}(14)_n\text{Mg}(\text{CF}_3\text{SO}_3)_2$ (b) mono-amidosils.

1710–1500 cm^{-1} interval (parts b and c of Figure 5, respectively). The frequency, integral area, and assignment of the resulting individual components are listed in Table S4 of the Supporting Information. Figure 6 shows the composition dependence of the integral area of the resolved components.

The amide I and amide II regions of the dilute $\text{m-A}(14)_n\text{KCF}_3\text{SO}_3$ ($n = 60$ and 20)/ $\text{m-A}(14)_n\text{Mg}(\text{CF}_3\text{SO}_3)_2$ ($n = 100$, 20 , and 10) mono-amidosils are dominated by intense bands centered at 1640/1639 and 1554 cm^{-1} , respectively (parts a and b of Figure S6 in the Supporting Information), corresponding to wavenumber differences ($\Delta\bar{\nu}$) of 86/85 cm^{-1} . In the case of the concentrated $\text{m-A}(14)_5\text{KCF}_3\text{SO}_3$ sample, the intensity maxima of the same bands shift to 1637 and 1549 cm^{-1} , respectively, but the $\Delta\bar{\nu}$ value remains practically unchanged (88 cm^{-1}) (Figure S6b in the Supporting Information). In the case of $\text{m-A}(14)_5\text{Mg}(\text{CF}_3\text{SO}_3)_2$, the amide I envelope becomes markedly broader and its profile is slightly different; however, its intensity maximum remains unshifted (1639 cm^{-1}) and $\Delta\bar{\nu} = 85 \text{ cm}^{-1}$. Considering that in the $\text{m-A}(14)$ matrix the amide I band is centered at 1640 cm^{-1} and the amide II band at 1551 cm^{-1} and thus $\Delta\bar{\nu} = 89 \text{ cm}^{-1}$,^{38,39} we are led to conclude the following: (1) Globally, the addition of KCF_3SO_3 and $\text{Mg}(\text{CF}_3\text{SO}_3)_2$ to $\text{m-A}(14)$ does not affect the strength of the original hydrogen bonded array of the host matrix. (2) In $\text{m-A}(14)_5\text{Mg}(\text{CF}_3\text{SO}_3)_2$, band redistribution occurs.

To get deeper insight into the hydrogen bonding interactions, we employed curve-fitting procedures to deconvolute the amide I and amide II envelopes of the KCF_3SO_3 - and $\text{Mg}(\text{CF}_3\text{SO}_3)_2$ -based mono-amidosils. The amide I and amide II bands of the $\text{m-A}(14)_n\text{KCF}_3\text{SO}_3$ and $\text{m-A}(14)_n\text{Mg}(\text{CF}_3\text{SO}_3)_2$ samples with $n \geq 20$ were resolved into four components at 1670, 1652–1654, 1639–1640, and 1624–1626 cm^{-1} and two components at 1561–1567 and 1545–1547 cm^{-1} , respectively (parts b and c of Figure 5, respectively, and

Table S4 in the Supporting Information). While the band at 1670 cm^{-1} is ascribed to non-bonded or “free” (F) C=O groups,^{38,39} that observed around 1652–1654 cm^{-1} is attributed to hydrogen-bonded C=O groups in disordered amide–amide aggregates (D).^{38,39} The events near 1639–1640 and 1624–1626 cm^{-1} are assigned to hydrogen-bonded C=O groups in ordered amide–amide aggregates (O1 and O2, respectively) of increasing strength.^{38,39} The two components located at approximately 1561–1567 and 1545–1547 cm^{-1} suggest that in this set of samples the hydrogen-bonded aggregates have two distinct degrees of order, a situation similar to that found in $\text{m-A}(14)$ (Figure 5a and Table S4 in the Supporting Information).^{38,39} The new amide I (1613 cm^{-1}) and amide II (1585 cm^{-1}) components detected in the FT-IR spectrum of $\text{m-A}(14)_5\text{Mg}(\text{CF}_3\text{SO}_3)_3$ (Figure 5c and Table S4 in the Supporting Information) may be correlated with the formation of very strong and ordered Mg^{2+} -coordinated amide–amide aggregates (O3). Interestingly, this phenomenon was also reported in the case of the $\text{m-A}(14)_n\text{Eu}(\text{CF}_3\text{SO}_3)_3$ analogues with $n \leq 20$.⁴² It is also important to note that, unlike in the case of $\text{m-A}(14)$ (Figure 5a and Table S4 in the Supporting Information),^{38,39} $\text{m-A}(14)_5\text{KCF}_3\text{SO}_3$ and $\text{m-A}(14)_5\text{Mg}(\text{CF}_3\text{SO}_3)_3$, in the dilute K^+ - and Mg^{2+} -doped $\text{m-A}(14)$ -based mono-amidosils with $n \geq 20$ non-bonded C=O groups are present (Figure 5b and c and Table S4 in the Supporting Information).

The plots of Figure 6 provide additional information about the modifications undergone by the various hydrogen-bonded aggregates of $\text{m-A}(14)$ upon introduction of increasing amounts of KCF_3SO_3 and $\text{Mg}(\text{CF}_3\text{SO}_3)_2$. It may be inferred from these graphs that the incorporation of these two guest salts into $\text{m-A}(14)$ ($n = 100$ and 60 , respectively) promotes the breakdown of aggregates O1 and an increase of both the fraction of aggregates O2 and of non-bonded C=O groups. In the case of $\text{m-A}(14)_{100}\text{Mg}(\text{CF}_3\text{SO}_3)_2$, the presence of salt also

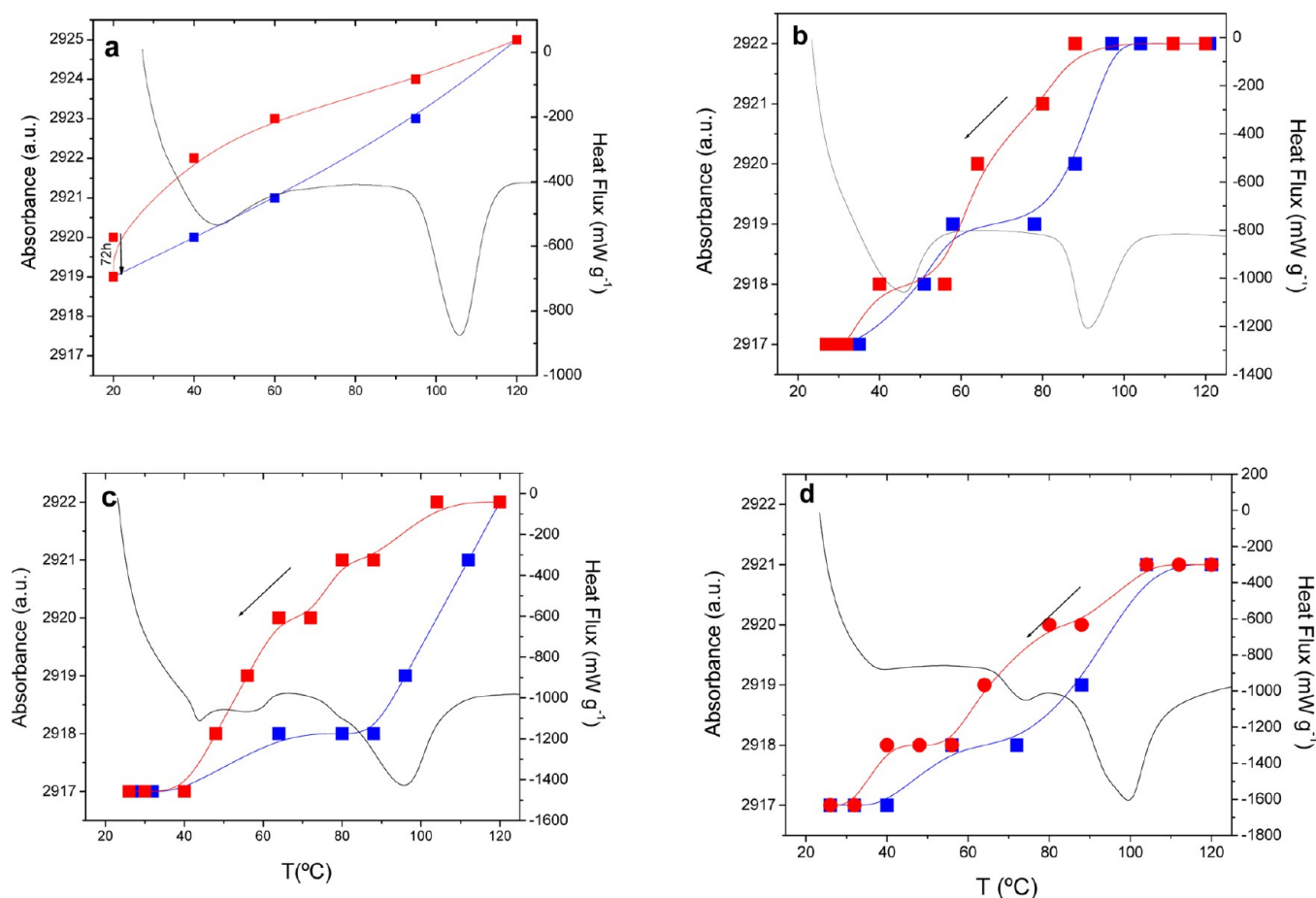


Figure 8. Temperature dependence of the frequency of the FT-IR/ATR ν_{CH_2} band (left axis, heating - blue line and cooling - red line) and DSC curve (right axis, black line) of m-A(14) (a) (adapted from ref 38), m-A(14)₂₀KCF₃SO₃ (b), m-A(14)₁₀₀Mg(CF₃SO₃)₂ (c), and m-A(14)₆₀(EuCF₃SO₃)₃ (d) mono-amidosils. The lines drawn are just guides for the eyes.

leads to the formation of more aggregates D (Figure 6b). Upon further addition of the salts ($n = 20$), the same trends continue, except that more aggregates O1 emerge. In parallel, a fraction of the aggregates D is destroyed. The main differences between both series of materials in terms of hydrogen bonding clearly arise at the highest salt concentration considered (Figure 6). In m-A(14)₅KCF₃SO₃, the C=O groups become saturated, the stronger aggregates O1 and O2 become dominant, and a marked reduction in the fraction of the weaker aggregates D results. In m-A(14)₅Mg(CF₃SO₃)₂, new aggregates (O3), more ordered than aggregates O1 and O2, are formed at the expense of the destruction of aggregates O1 (Figure 6b).

To further clarify the local environment of the cations and to elucidate the extent of ionic association and consequently determine the nature of the anionic configurations formed in the two series of mono-amidosils investigated, the FT-IR spectra of the m-A(14)_nKCF₃SO₃ and m-A(14)_nMg(CF₃SO₃)₂ mono-amidosils were analyzed through the inspection of a characteristic band of the anion which is sensitive to coordination effects: the non-degenerate symmetric stretching vibration ($\nu_{\text{s}}\text{SO}_3$) mode of the triflate ion. When the anion is “free”, this mode is located at 1032 cm⁻¹.⁶³ While shifts of the $\nu_{\text{s}}\text{SO}_3$ band to lower and higher wavenumbers may occur upon coordination of the triflate ion to the Mg²⁺ ion,^{64,65} upon interaction with the K⁺ ion the $\nu_{\text{s}}\text{SO}_3$ is shifted to higher wavenumbers.^{66,67}

The FT-IR spectra of the m-A(14)_nKCF₃SO₃ and m-A(14)_nMg(CF₃SO₃)₂ mono-amidosils in the $\nu_{\text{s}}\text{SO}_3$ region are represented in parts a and b of Figure S7 in the Supporting Information, respectively. The results of the curve-fitting performed in the 1085–1010 cm⁻¹ interval are reproduced in parts a and b of Figure 7, respectively. The FT-IR $\nu_{\text{s}}\text{SO}_3$ mode of the K⁺-doped mono-amidosils with $n \geq 20$ and of the m-A(14)₂₀Mg(CF₃SO₃)₂ sample was decomposed into three components: a band at 1031 cm⁻¹ and two shoulders around 1027 and 1036–1038 cm⁻¹ (Figure 7). In the mono-amidosils m-A(14)₅KCF₃SO₃ and m-A(14)₁₀Mg(CF₃SO₃)₂, a new component is evident at 1041 cm⁻¹ (Figure 7a) and at 1045 cm⁻¹ (Figure 7b), respectively. Additionally, in the FT-IR $\nu_{\text{s}}\text{SO}_3$ region of the most concentrated m-A(14)₅Mg(CF₃SO₃)₂ material, three new components emerge at 1054 and 1065 cm⁻¹ (Figure 7b) and another one, very weak, at 1099 cm⁻¹ (not shown).

The presence of the 1031 cm⁻¹ band in the FT-IR spectra of all the K⁺/Mg²⁺-doped mono-amidosil samples confirms the occurrence of “free” anions.^{63,68} It is likely that this band also receives the contribution of “cross-link-separated ion pair” species.⁶⁹ The shoulders produced at ca. 1027 and 1036/1038 cm⁻¹ in the K⁺/Mg²⁺-doped m-A(14) with $n \geq 20$ are associated with weakly coordinated triflate ions located in two different types of environments:⁶⁹ (1) CF₃SO₃⁻ species weakly bonded to the K⁺/Mg²⁺ ions, which simultaneously interact with the C=O oxygen atoms of the amide groups; (ii)

CF_3SO_3^- ions hydrogen-bonded to the amide N—H groups. This conclusion is beautifully corroborated by the EDS data obtained for $\text{m-A}(14)_{20}\text{KCF}_3\text{SO}_3$ (Figure 3c), which reveal a non-homogenous distribution for the K^+ ions. In the FT-IR spectra of $\text{m-A}(14)_5\text{KCF}_3\text{SO}_3/\text{m-A}(14)_n\text{Mg}(\text{CF}_3\text{SO}_3)_2$ with $n \leq 5/10$, the $1041/1045\text{ cm}^{-1}$ feature, respectively, is ascribed to contact ion pairs.⁶⁶ The 1054 and 1065 cm^{-1} components produced by $\text{m-A}(14)_5\text{Mg}(\text{CF}_3\text{SO}_3)_2$ are associated with higher ionic aggregates, whereas the event at 1099 cm^{-1} confirms the presence of free $\text{Mg}(\text{CF}_3\text{SO}_3)_2$.⁷⁰

The study of the amide I region of the K^+ , Mg^{2+} , and Eu^{3+} -doped mono-amidosils clearly demonstrated that the carbonyl environments ("free" $\text{C}=\text{O}$ groups and hydrogen-bonded aggregates) of the salt-free framework are less perturbed by the inclusion of KCF_3SO_3 and $\text{Mg}(\text{CF}_3\text{SO}_3)_2$ than by the incorporation of $\text{Eu}(\text{CF}_3\text{SO}_3)_3$.⁴² For instance, while in the $\text{m-A}(14)_n\text{Eu}(\text{CF}_3\text{SO}_3)_3$ materials, no "free" $\text{C}=\text{O}$ groups remain available for coordination purposes at $n = 20$;⁴² in the case of the hybrids doped with K^+ and Mg^{2+} ions, the saturation of the amide cross-links is attained at much higher salt content ($n = 5$).

The information retrieved from the FT-IR $\nu_s\text{SO}_3$ region revealed that the local chemical surrounding of the triflate ions in the $\text{m-A}(14)_n\text{KCF}_3\text{SO}_3$, $\text{m-A}(14)_n\text{Mg}(\text{CF}_3\text{SO}_3)_2$, and $\text{m-A}(14)_n\text{Eu}(\text{CF}_3\text{SO}_3)_3$ systems is very similar for $n \geq 20$, independently of the type of cation included. The only anionic environments detected in these samples were "free" ions and weakly coordinated triflate ions, an indication that the degree of ionic association is very low in this composition range. Contact ion pairs are formed in the three series of mono-amidosils at higher salt content. In addition, these spectroscopic data suggest that the salt-rich sample $\text{m-A}(14)_5\text{Mg}(\text{CF}_3\text{SO}_3)_2$ has a considerably higher tendency than $\text{m-A}(14)_5\text{KCF}_3\text{SO}_3$ to form associated species (high ionic aggregates and free salt).

Temperature Dependence of the Order/Disorder Phase Transitions. The observation of two endothermic features at about 90 and 40°C in the DSC curves of the K^+ - and Mg^{2+} -doped mono-amidosils with $n \geq 5$ and $n \geq 20$, respectively, induced us to examine in more detail the order/disorder phase transitions. With this goal, we monitored by FT-IR/ATR the changes experienced by the $\nu_a\text{CH}_2$ mode of $\text{m-A}(14)_{20}\text{KCF}_3\text{SO}_3$, $\text{m-A}(14)_{100}\text{Mg}(\text{CF}_3\text{SO}_3)_2$, and $\text{m-A}(14)_{60}\text{Eu}(\text{CF}_3\text{SO}_3)_3$ during a heating/cooling cycle between room temperature and 120°C . These samples were chosen because, according to the FT-IR data discussed above, they have the great majority of the alkyl chains in *all-trans* conformations. The results of this spectroscopic study in the $\nu_a\text{CH}_2$ region are represented in the plots in Figures 8b, c, and d, together with the DSC curves obtained for each sample. We must emphasize, however, that, while the FT-IR measurements are sensitive to local conformational changes of neighboring alkyl chains, the DSC measurements provide information about the thermal changes undergone by alkyl chains at a supra-molecular level. Moreover, the time scale of the measurements is not the same. The temperature dependence of the $\nu_a\text{CH}_2$ mode is reproduced in parts b, c, and d of Figures S8 in the Supporting Information, respectively.

Upon heating $\text{m-A}(14)_{20}\text{KCF}_3\text{SO}_3$ and $\text{m-A}(14)_{100}\text{Mg}(\text{CF}_3\text{SO}_3)_2$, the FT-IR $\nu_a\text{CH}_2$ band shifted from 2917 to 2922 cm^{-1} (blue lines in Figure 8b and c). This proves that the population of *gauche* conformers progressively increases, until the organic chains become disordered, resembling the liquid *n*-alkanes phase.^{35,52,56,57} Upon subsequent cooling down to

room temperature, the frequency of the FT-IR $\nu_a\text{CH}_2$ band returns to the initial value (red lines in Figure 8b and c), indicating that the alkyl chains recovered the *all-trans*, ordered state. These findings demonstrate not only that the thermally induced structural changes undergone by the alkyl chains are reversible but also that they are time-independent. Nevertheless, the most interesting effect revealed by the curves of Figures 8b and c is undoubtedly the existence of two distinct hysteresis domains, one definitely associated with the order/disorder phase transition of the original lamellar structure of $\text{m-A}(14)$ (characteristic temperature of ca. 90°C) (Figure 8a) and the second one associated with the order/disorder phase transition of the new lamellar structure which emerged in the presence of the guest salts (characteristic temperature of ca. 40°C). The $\text{m-A}(14)_{60}\text{Eu}(\text{CF}_3\text{SO}_3)_3$ sample exhibits a similar effect (Figure 8d), although the hysteresis appears to be less pronounced than in the $\text{m-A}(14)_{20}\text{KCF}_3\text{SO}_3$ and $\text{m-A}(14)_{100}\text{Mg}(\text{CF}_3\text{SO}_3)_2$ materials. The latter effect may be due to the fact that, in the case of the Eu^{3+} -doped mono-amidosil, the characteristic temperatures of the two order/disorder phase transitions are very close.⁴² Unfortunately, no conclusions concerning the behavior of the hydrogen-bonded array after the heating/cooling cycle could be retrieved from the FT-IR/ATR data, due to the low signal/noise ratio of the spectra in the amide I and amide II regions.

CONCLUSIONS

In the present work, three series of ordered hybrid materials, produced by the sol-gel process and self-directed assembly, comprising the $\text{m-A}(14)$ mono-amidosil host hybrid network and a wide concentration of KCF_3SO_3 , $\text{Mg}(\text{CF}_3\text{SO}_3)_2$, and $\text{Eu}(\text{CF}_3\text{SO}_3)_3$, were investigated. The morphology of the doped materials depends on the nature of the guest cation. Structurally, the presence of the K^+ , Mg^{2+} , and Eu^{3+} ions results, for $n \geq 5$, 20 , and 60 (where n is the molar ratio of amide $\text{C}=\text{O}$ groups per cation), respectively, in the formation of a new lamellar bilayer phase which coexists with the original lamellar bilayer structure of $\text{m-A}(14)$. From the standpoint of interactions, the addition of the alkaline, alkaline-earth, and lanthanide triflate salts to $\text{m-A}(14)$ has two major consequences: (1) The hydrogen-bonded array of all the materials is partially destroyed as a result of the coordination of the cations to the oxygen atoms of the amide cross-links, the effect being particularly important in the case of $\text{Eu}(\text{CF}_3\text{SO}_3)_3$. (2) The degree of ionic association is low for $n \geq 20$. Contact ion pairs develop at higher salt concentration, and crystalline salt is formed only in the samples doped with $\text{Mg}(\text{CF}_3\text{SO}_3)_2$ and $\text{Eu}(\text{CF}_3\text{SO}_3)_3$ and $n = 5$ and 10 , respectively. During a heating/cooling cycle, the structural modifications undergone by the alkyl chains of selected samples are reversible and time-independent. Owing to the existence of two lamellar bilayer structures, two distinct hysteresis domains, associated with the respective order/disorder phase transitions, are evident. The present investigation is clearly worth pursuing, as several questions remain unanswered. For instance, the composition of the first coordination shell around the three cations as well as the bonding geometry of the triflate ion (mono-, di-, or tridentate) in the samples examined are unknown. Another issue which needs to be elucidated in more detail is the coordination of the cations to the Si—OH groups. Complementary information obtained from additional data, such as Raman, EXAFS, and photoluminescence, are thus required. PL measurements will also be a precious tool to revisit the order/

disorder phase transition of the $m\text{-A}(14)_n(\text{EuCF}_3\text{SO}_3)_3$ mono-amidosils.

■ ASSOCIATED CONTENT

■ Supporting Information

Synthesis procedure of the $m\text{-A}(14)_n\text{KCF}_3\text{SO}_3$ and $m\text{-A}(14)_n\text{Mg}(\text{CF}_3\text{SO}_3)_2$ mono-amidosils; details of the synthesis procedure of the $m\text{-A}(14)_n\text{KCF}_3\text{SO}_3$ and $m\text{-A}(14)_n\text{Mg}(\text{CF}_3\text{SO}_3)_2$ mono-amidosils; FT-IR in the $\nu_a\text{CH}_2$, $\nu_s\text{SO}_3$, amide I, and amide II and $\nu_s\text{SO}_3$ regions of $m\text{-A}(14)$ and of the $m\text{-A}(14)_n\text{KCF}_3\text{SO}_3$ and $m\text{-A}(14)_n\text{Mg}(\text{CF}_3\text{SO}_3)_2$ mono-amidosils; ^{13}C CP/MAS and ^{29}Si MAS NMR spectra of $m\text{-A}(14)$ and of selected $m\text{-A}(14)_n\text{KCF}_3\text{SO}_3$ and $m\text{-A}(14)_n\text{Mg}(\text{CF}_3\text{SO}_3)_2$ mono-amidosils; XRD patterns, DSC curves, and TGA curves of KCF_3SO_3 and $\text{Mg}(\text{CF}_3\text{SO}_3)_2$; TGA and derivative curves of selected $m\text{-A}(14)_n\text{KCF}_3\text{SO}_3$ and $m\text{-A}(14)_n\text{Mg}(\text{CF}_3\text{SO}_3)_2$ mono-amidosils. This material is available free of charge via the Internet at <http://pubs.acs.org>.

■ AUTHOR INFORMATION

Corresponding Authors

*Phone: +351-275-242021. Fax: +351-275-319730. E-mail: snunes@ubi.pt.

*Phone: +351-259-350253. Fax: +351-259-350480. E-mail: vbermude@utad.pt.

Notes

The authors declare no competing financial interest.

■ ACKNOWLEDGMENTS

This work was supported by Fundação para a Ciência e a Tecnologia (FCT) and FEDER (contracts PTDC/CTM/101324/2008, PTDC/QUI-QUI/100896/2008, PTDC/CTM-BPC/112774/2009, Pest-C/SAU/UI0709/2011, and Pest-14C/CTM/LA0013/2013) and COST Action MP1202 "Rational design of hybrid organic-inorganic interfaces". S.C.N. acknowledges FCT for a grant (SFRH/BPD/63152/2009). The authors are grateful to Dr. Denis Ostrovskii of the Department of Applied Physics, Chalmers University of Technology, Göteborg, Sweden, for recording the FT-IR spectra.

■ REFERENCES

- (1) Sanchez, C.; Gomez Romero, P., Eds. *Functional Hybrid Materials*; Wiley Interscience: New York, 2003.
- (2) Kiclick, G. *Hybrid Materials: Synthesis, Characterization and Applications*; Wiley-VCH: Weinheim, Germany, 2007.
- (3) Boury, B.; Corriu, R. J. P.; Le Strat, V.; Delord, P.; Nobili, M. Nanostructured Silica-Based Organic-Inorganic Hybrid Materials: Evidence for Self-Organization of a Xerogel Prepared by Sol-Gel Polymerization. *Angew. Chem., Int. Ed.* **1999**, *38*, 3172–3173.
- (4) Corriu, R. J. P. Ceramics and Nanostructures from Molecular Precursors. *Angew. Chem., Int. Ed.* **2000**, *39*, 1376–1398.
- (5) Boury, B.; Corriu, R. J. P. Auto-organisation of Hybrid Organic-Inorganic Materials Prepared by Sol-gel Process. *Chem. Commun.* **2002**, 795–802.
- (6) Ben, F.; Boury, B.; Corriu, R. J. P.; Delord, P.; Nobili, M. Control of the Anisotropic Organization of Nanostructured Silica-Based Hybrid Materials. *Chem. Mater.* **2002**, *14*, 730–738.
- (7) Kresge, C. T.; Leonowicz, M. E.; Roth, W. J.; Vartulli, J. C.; Beck, J. S. Ordered Mesoporous Molecular Sieves Synthesized by a Liquid-Crystal Template Mechanism. *Nature* **1992**, *359*, 710–712.
- (8) Lu, Y.; Ganguli, R.; Drewien, C. A.; Anderson, M. T.; Brinker, C. J.; Gong, W.; Guo, Y.; Soyez, H.; Dunn, B.; Huang, M. H.; Zink, J. I. Continuous Formation of Supported Cubic and Hexagonal Mesoporous Films by Sol-Gel Dip-Coating. *Nature* **1997**, *389*, 364–368.
- (9) Shea, K. J.; Loy, D. A.; Webster, O. W. Arylsilsesquioxane Gels and Related Materials. New hybrids of Organic and Inorganic Networks. *J. Am. Chem. Soc.* **1992**, *114*, 6700–6710.
- (10) Loy, D. A.; Shea, K. J. Bridged Polysilsesquioxanes. Highly Porous Hybrid Organic-Inorganic Materials. *Chem. Rev.* **1995**, *95*, 1431–1442.
- (11) Shea, K. J.; Loy, D. A. Bridged Polysilsesquioxanes. Molecular-Engineered Hybrid Organic-Inorganic Materials. *Chem. Mater.* **2001**, *13*, 3306–3319.
- (12) Sanchez, C.; Julián, B.; Belleville, P.; Popall, M. Applications of Hybrid Organic-Inorganic Nanocomposites. *J. Mater. Chem.* **2005**, *15*, 3559–3592.
- (13) Sanchez, C.; Belleville, P.; Popall, M.; Nicole, L. Applications of Advanced Hybrid Organic-Inorganic Nanomaterials: from Laboratory to Market. *Chem. Soc. Rev.* **2011**, *40*, 696–753.
- (14) Brinker, C. J.; Scherer, G. W. *Sol-gel Science: the Physics and Chemistry of Sol-gel Processing*; Academic Press: San Diego, CA, 1990.
- (15) Bied, C.; Gauthier, D.; Moreau, J. J. E.; Wong Chi Man, M. Preparation and Characterization of New Templated Hybrid Materials Containing a Chiral Diamine Ligand. *J. Sol-Gel Sci. Technol.* **2001**, *20*, 313–320.
- (16) Moreau, J. J. E.; Vellutini, L.; Wong Chi Man, M.; Bied, C.; Bantignies, J.-L.; Dieudonné, P.; Sauvajol, J.-L. Self-Organized Hybrid Silica with Long-Range Ordered Lamellar Structure. *J. Am. Chem. Soc.* **2001**, *123*, 7957–7958.
- (17) Moreau, J. J. E.; Vellutini, L.; Bied, C.; Wong Chi Man, M.; Bied, C.; Bantignies, J.-L.; Sauvajol, J.-L. New Approach for the Organisation and the Shaping of Organo-Bridged Silicas: An Overview. *J. Sol-Gel Sci. Technol.* **2004**, *31*, 151–156.
- (18) Moreau, J. J. E.; Vellutini, L.; Wong Chi Man, M.; Bied, C.; Bantignies, J.-L.; Sauvajol, J.-L. Lamellar Bridged Silsesquioxanes: Self-Assembly through a Combination of Hydrogen Bonding and Hydrophobic Interactions. *Chem. Eur. J.* **2005**, *11*, 1527–1537.
- (19) Moreau, J. J. E.; Pichon, B. P.; Wong Chi Man, M.; Bied, C.; Prizkow, H.; Bantignies, J.-L.; Dieudonné, P.; Sauvajol, J.-L. A Better Understanding of the Self-Structuration of Bridged Silsesquioxanes. *Angew. Chem., Int. Ed.* **2004**, *43*, 203–206.
- (20) Moreau, J. J. E.; Pichon, B. P.; Bied, C.; Wong Chi Man, M. Structuring of Bridged Silsesquioxanes via Cooperative Weak Interactions: H-bonding of Urea Groups and Hydrophobic Interactions of Long Alkylene Chains. *J. Mater. Chem.* **2005**, *15*, 3929–3936.
- (21) Nobre, S. S.; Brites, C. D. S.; Ferreira, R. A. S.; de Zea Bermudez, V.; Carcel, C.; Moreau, J. J. E.; Rocha, J.; Wong Chi Man, M.; Carlos, L. D. Photoluminescence of Eu(III)-doped lamellar bridged silsesquioxanes self-templated through a hydrogen bonding array. *J. Mater. Chem.* **2008**, *18*, 4172–4182.
- (22) Nobre, S. S.; Cattoën, X.; Ferreira, R. A. S.; Carcel, C.; de Zea Bermudez, V.; Wong Chi Man, M.; Carlos, L. D. Eu³⁺-Assisted Short-Range Ordering of Photoluminescent Bridged Silsesquioxanes. *Chem. Mater.* **2010**, *22*, 3599–3609.
- (23) Besson, E.; Mehdi, A.; Reye, C.; Gaveau, P.; Corriu, R. P. Self-assembly of Layered Organosilicas Based on Weak Intermolecular Interactions. *Dalton Trans.* **2010**, 39, 7534–7539.
- (24) Fernandes, M.; Nobre, S. S.; Qinghong, X.; Carcel, C.; Cachia, J. N.; Cattoën, X.; Sousa, J. M.; Ferreira, R. A. S.; Carlos, L. D.; Santilli, C. V.; Wong Chi Man, M.; de Zea Bermudez, V. Self-structuring of Lamellar Bridged Silsesquioxanes with Long Side Spacers. *J. Phys. Chem. B* **2011**, *115*, 10877–10891.
- (25) Fernandes, M.; Cattoën, X.; de Zea Bermudez, V.; Wong Chi Man, M. Solvent-Controlled Morphology of Lamellar Silsesquioxanes: from Platelets to Microsponges. *CrystEngComm* **2011**, *13*, 1410–1415.
- (26) Zhou, X.; Yang, S.; Yu, C.; Li, Z.; Yan, X.; Cao, Y.; Zhao, D. Hexylene- and Octylene-Bridged Polysilsesquioxane Hybrid Crystals Self-Assembled by Dimeric Building Blocks with Ring Structures. *Chem. Eur. J.* **2006**, *12*, 8484–8490.

- (27) Inagaki, S.; Guan, S.; Ohsuna, T.; Terasaki, O. An Ordered Mesoporous Organosilica Hybrid Material with a Crystal-like Wall Structure. *Nature* **2002**, *416*, 304–307.
- (28) Shimojima, A.; Sugahara, Y.; Kuroda, K. Inorganic–Organic Layered Materials Derived via the Hydrolysis and Polycondensation of Trialkoxy(alkyl)silanes. *Bull. Chem. Soc. Jpn.* **1997**, *70*, 2847–2853.
- (29) Shimojima, A.; Kuroda, K. Controlled Synthesis of Nanostructured Silica-based Materials from Designed Alkoxysilanes. *J. Sol-Gel Sci. Technol.* **2008**, *46*, 307–311.
- (30) Shimojima, A.; Kuroda, K. Designed synthesis of nanostructured siloxane-organic hybrids from amphiphilic silicon-based precursors. *Chem. Rec.* **2006**, *6*, 53–63.
- (31) Fujimoto, Y.; Shimojima, A.; Kuroda, K. Formation of Layered Silica-Alcohol Nanostructured Materials from Alkoxytrichlorosilanes. *Chem. Mater.* **2003**, *15*, 4768–4774.
- (32) Shimojima, A.; Kuroda, K. Direct Formation of Mesostructured Silica-Based Hybrids from Novel Siloxane Oligomers with Long Alkyl Chains. *Angew. Chem., Int. Ed.* **2003**, *42*, 4057–4060.
- (33) Shimojima, A.; Liu, Z.; Ohsuna, T.; Terasaki, O.; Kuroda, K. Self-Assembly of Designed Oligomeric Siloxanes with Alkyl Chains into Silica-Based Hybrid Mesostructures. *J. Am. Chem. Soc.* **2005**, *127*, 14108–14116.
- (34) Sakamoto, S.; Shimojima, A.; Miyasaka, K.; Ruan, J.; Terasaki, O.; Kuroda, K. Formation of Two- and Three-Dimensional Hybrid Mesostructures from Branched Siloxane Molecules. *J. Am. Chem. Soc.* **2009**, *131*, 9634–9635.
- (35) Parikh, A. N.; Schivley, M. A.; Koo, E.; Seshadri, K.; Aurentz, D.; Mueller, K.; Allara, D. L. *n*-Alkylsiloxanes: From Single Monolayers to Layered Crystals. The Formation of Crystalline Polymers from the Hydrolysis of *n*-Octadecyltrichlorosilane. *J. Am. Chem. Soc.* **1997**, *119*, 3135–3143.
- (36) Nakazaki, Y.; Fujita, K.; Tanaka, K.; Uchino, T. Effect of Microscopic Structure and Porosity on the Photoluminescence Properties of Silica Gels. *J. Phys. Chem. C* **2008**, *112*, 10878–10882.
- (37) Nishimura, A.; Harada, S.; Uchino, T. Effect of Cross-Linking and Organic Groups on the Visible Photoluminescence Characteristics of *n*-Octadecylsiloxanes. *J. Phys. Chem. C* **2010**, *114*, 8568–8574.
- (38) Carlos, L. D.; de Zea Bermudez, V.; Amaral, V. S.; Nunes, S. C.; Silva, N. J. O.; Ferreira, R. A. S.; Santilli, C. V.; Ostrovskii, D.; Rocha, J. Nanoscopic Photoluminescence Memory as a Fingerprint of Complexity in Self-Assembled Alkyl/Siloxane Hybrids. *Adv. Mater.* **2007**, *19*, 341–348.
- (39) Nunes, S. C. Ph.D. Dissertation, 2007, Vila Real (Portugal), 92678/1/2 SD (<http://opac.sde.utad.pt/geral>).
- (40) Nunes, S. C.; Silva, N. J. O.; Hümmer, J.; Ferreira, R. A. S.; Almeida, P.; Carlos, L. D.; de Zea Bermudez, V. Water-mediated Structural Tunability of an Alkyl/Siloxane Hybrid: from Amorphous Material to Lamellar Structure or Bilamellar Superstructure. *RSC Adv.* **2012**, *2*, 2087–2099.
- (41) Fernandes, M.; Cattoën, X.; Ferreira, R. A. S.; Carlos, L. D.; W. Chi Man, M.; de Zea Bermudez, V. Photoluminescent Lamellar Bilayer Mono-alkyl-Urethanesils. *J. Sol-Gel Sci. Technol.* **2013**, *65*, 61–73.
- (42) Nunes, S. C.; Planelles-Aragó, J.; Ferreira, R. A. S.; Carlos, L. D.; de Zea Bermudez, V. Eu^{III}-Doping of Lamellar Bilayer and Amorphous Mono-Amide Cross-Linked Alkyl/Siloxane Hybrids. *Eur. J. Inorg. Chem.* **2010**, *18*, 2688–2699.
- (43) Nunes, S. C.; Ferreira, C. B.; Hümmer, J.; Ferreira, R. A. S.; Carlos, L. D.; Almeida, P.; de Zea Bermudez, V. Lamellar Mono-amidosil Hybrids Incorporating Monomethinecyanine Dyes. *J. Mater. Chem. C* **2013**, *1*, 2290–2301.
- (44) Teixeira, J. C. S.; Fernandes, M.; de Zea Bermudez, V.; Barbosa, P. C.; Rodrigues, L. C.; Silva, M. M.; Smith, M. J. Mg²⁺-doped Poly(*ε*-caprolactone)/Siloxane Biohybrids. *Electrochim. Acta* **2010**, *55*, 1328–1332.
- (45) Peakfit is a product of Jandel Corporation, 2591 Rerner Boulevard, San Rafael, CA 94901, USA.
- (46) Clauss, J.; Schmidt-Rohr, K.; Adam, A.; Boeffel, C.; Spiess, H. W. S. Macromolecules with Aliphatic Side Chains: Side-chain Mobility, Conformation, and Organization from 2D Solid-State NMR Spectroscopy. *Macromolecules* **1992**, *25*, 5208–5214.
- (47) Wang, L.-Q.; Liu, J.; Exarhos, G. J.; Flanigan, K. Y.; Bordia, R. Conformation Heterogeneity and Mobility of Surfactant Molecules in Intercalated Clay Minerals Studied by Solid-State NMR. *J. Phys. Chem. B* **2000**, *104*, 2810–2816.
- (48) Carlos, L. D.; de Zea Bermudez, V.; Ferreira, R. A. S.; Marques, L.; Assunção, M. Sol-Gel Derived Urea Cross-Linked Organically Silicates. Blue Light Emission. *Chem. Mater.* **1999**, *11*, 581–588.
- (49) Boehm, C.; Leveiller, F.; Jacquemain, D.; Mohwald, H.; Kjaer, K.; Als-Nielsen, J.; Weissbuch, I.; Leiserowitz, L. Packing Characteristics of Crystalline Monolayers of Fatty Acid Salts, at the Air-Solution Interface, Studied by Grazing Incidence X-ray Diffraction. *Langmuir* **1994**, *10*, 830–836.
- (50) Nagle, J. F.; Goldstein, M. Decomposition of Entropy and Enthalpy for the Melting Transition of Polyethylene. *Macromolecules* **1985**, *18*, 2643–2652.
- (51) Porter, M. D.; Bright, T. B.; Allara, D. L.; Childsey, C. E. D. Spontaneously Organized Molecular Assemblies. 4. Structural Characterization of *n*-Alkyl Thiol Monolayers on Gold by Optical Ellipsometry, Infrared Spectroscopy, and Electrochemistry. *J. Am. Chem. Soc.* **1987**, *109*, 3559–3568.
- (52) Singh, S.; Wegmann, J.; Albert, K.; Müller, K. Variable Temperature FT-IR Studies of *n*-Alkyl Modified Silica Gel. *J. Phys. Chem. B* **2002**, *106*, 878–883.
- (53) Venkataram, N. V.; Vasudevan, S. Interdigitation of an Intercalated Surfactant Bilayer. *J. Phys. Chem. B* **2001**, *105*, 7639–7650.
- (54) Venkataram, N. V.; Bhagyalakshmi, S.; Vasudevan, S.; Seshachi, R. Conformation and Orientation of Alkyl Chains in the Layered Organic–Inorganic Hybrids: (C_nH_{2n+1}NH₃)₂PbI₄ (*n* = 12, 16, 18). *J. Phys. Chem. Chem. Phys.* **2002**, *4*, 4533–4538.
- (55) Wang, R.; Baran, G.; Wunder, S. L. Packing and Thermal Stability of Polyoctadecylsiloxane Compared with Octadecylsilane Monolayers. *Langmuir* **2000**, *16*, 6298–6305.
- (56) Macphail, R. A.; Strauss, H. L.; Snyder, R. G.; Ellinger, C. A. Carbon-hydrogen Stretching Modes and the Structure of *n*-alkyl Chains. 2. Long, all-trans Chains. *J. Phys. Chem.* **1984**, *88*, 334–341.
- (57) Snyder, R. G.; Strauss, H. L.; Ellinger, C. A. C-H Stretching Modes and the Structure of *n*-Alkyl Chains. 1. Long, Disordered Chains. *J. Phys. Chem.* **1982**, *86*, 5145–5150.
- (58) Douglas, B.; McDaniel, D.; Alexander, J. *Concepts and Models of Inorganic Chemistry*, 3rd ed.; John Wiley & Sons: New York, 1994.
- (59) Miyazawa, T.; Shimanouchi, T.; Mizushima, S.-I. Characteristic Infrared Bands of Monosubstituted Amides. *J. Chem. Phys.* **1956**, *24* (2), 408–419.
- (60) Skrovanek, D. J.; Howe, S. E.; Painter, P. C.; Coleman, M. M. Hydrogen Bonding in Polymers: Infrared Temperature Studies of an Amorphous Polyamide. *Macromolecules* **1985**, *18*, 1676–1883.
- (61) Skrovanek, D. J.; Painter, P. C.; Coleman, M. M. Hydrogen Bonding in Polymers. 2. Infrared Temperature Studies of Nylon 11. *Macromolecules* **1986**, *19*, 699–705.
- (62) Coleman, M. M.; Lee, K. H.; Skrovanek, D. J.; Painter, P. C. Hydrogen Bonding in Polymers. 4. Infrared Temperature Studies of a simple Polyurethane. *Macromolecules* **1986**, *19*, 2149–2157.
- (63) Wendsjö, Å.; Lindgren, J.; Thomas, J. O.; Farrington, G. C. The Effect of Temperature and Concentration on the Local Environment in the System M(CF₃SO₃)₂PEO_{*n*} for M=Ni, Zn and Pb. *Solid State Ionics* **1992**, *53–56*, 1077–1082.
- (64) Gonçalves, M. C.; de Zea Bermudez, V.; Ostrovskii, D.; Carlos, L. D. Cationic and Anionic Environments in Mono-Urethanesil Hybrids doped with Magnesium Triflate. *Solid State Ionics* **2004**, *166* (1–2), 103–114.
- (65) Nunes, S. C.; de Zea Bermudez, V.; Ostrovskii, D.; Carlos, L. D. Di-ureasil Ormolytes doped with Mg²⁺ ions: Part 2. Cationic and Anionic Environments. *Solid State Ionics* **2005**, *176*, 1601–1611.
- (66) Chintapalli, S.; Quinton, C.; Frech, R.; Vincent, C. A. Compound Formation and Ionic Association in the Poly(ethylene

oxide)—Potassium Triflate System. *Macromolecules* **1997**, *30*, 7472–7477.

(67) Nunes, S. C.; de Zea Bermudez, V.; Silva, M. M.; Smith, M. J.; Ostrovskii, D.; Ferreira, R. A. S.; Carlos, L. D.; Rocha, J.; Gonçalves, A.; Fortunato, E. Sol–gel-derived Potassium-based Di-ureasils for “Smart Windows. *J. Mater. Chem.* **2007**, *17*, 4239–4248.

(68) Petersen, G.; Brodin, A.; Torell, L. M.; Smith, M. J. Light Scattering and Luminescence Studies of $M(\text{CF}_3\text{SO}_3)_x$ -Polyether Complexes Containing Trivalent Cations. *Solid State Ionics* **1994**, *72*, 165–171.

(69) de Zea Bermudez, V.; Ostrovskii, D.; Lavoryk, S.; Gonçalves, M. C.; Carlos, L. D. Urethane Cross-linked Poly(oxyethylene)/Siliceous Nanohybrids doped with Eu^{3+} ions. Part I: Ion Association. *Phys. Chem. Chem. Phys.* **2004**, *6* (3), 649–658.

(70) Ostrovskii, D.; Nunes, S. C.; de Zea Bermudez, V. Unpublished results.